Nonequilibrium Thermodynamics of Porous Electrodes

Todd R. Ferguson[1] and Martin Z. Bazant[1,2]

[1] *Department of Chemical Engineering, Massachusetts Institute of Technology*
[2] *Department of Mathematics, Massachusetts Institute of Technology*

(Dated: April 16, 2012)

We review classical porous electrode theory and extend it to non-ideal active materials, including those capable of phase transformations. Using principles of non-equilibrium thermodynamics, we relate the cell voltage, ionic fluxes, and Faradaic charge-transfer kinetics to the variational electrochemical potentials of ions and electrons. The Butler-Volmer exchange current is consistently expressed in terms of the activities of the reduced, oxidized and transition states, and the activation overpotential is defined relative to the local Nernst potential. We also apply mathematical bounds on effective diffusivity to estimate porosity and tortuosity corrections. The theory is illustrated for a Li-ion battery with active solid particles described by a Cahn-Hilliard phase-field model. Depending on the applied current and porous electrode properties, the dynamics can be limited by electrolyte transport, solid diffusion and phase separation, or intercalation kinetics. In phase-separating porous electrodes, the model predicts narrow reaction fronts, mosaic instabilities and voltage fluctuations at low current, consistent with recent experiments, which could not be described by existing porous electrode models.

I. INTRODUCTION

Modeling is a key component of any design process. An accurate model allows one to interpret experimental data, identify rate limiting steps and predict system behavior, while providing a deeper understanding of the underlying physical processes. In systems engineering, empirical models with fitted parameters are often used for design and control, but it is preferable, whenever possible, to employ models based on microscopic physical or geometrical parameters, which can be more easily interpreted and optimized.

In the case of electrochemical energy storage devices, such as batteries, fuel cells, and supercapacitors, the systems approach is illustrated by equivalent circuit models, which are widely used in conjunction with impedance spectroscopy to fit and predict cell performance and degradation. This approach is limited, however, by the difficulty in unambiguously interpreting fitted circuit elements and in making predictions for the nonlinear response to large operating currents. There is growing interest, therefore, in developing physics-based porous electrode models and applying them for battery optimization and control [102]. Quantum mechanical computational methods have demonstrated the possibility of predicting bulk material properties, such as open circuit potential and solid diffusivity, from first principles [39], but coarse-grained continuum models are needed to describe the many length and time scales of interfacial reactions and multiphase, multicomponent transport phenomena.

Mathematical models could play a crucial role in guiding the development of new intercalation materials, electrode microstructures, and battery architectures, in order to meet the competing demands in power density and energy density for different envisioned applications, such as electric vehicles or renewable (e.g. solar, wind) energy storage. Porous electrode theory, pioneered by J. Newman and collaborators, provides the standard modeling framework for battery simulations today [93]. As reviewed in the next section, this approach has been developed for over half a century and applied successfully to many battery systems. The treatment of the active material, however, remains rather simple, and numerous parameters are often needed to fit experimental data.

In porous electrode theory for Li-ion batteries, the solid active particles are modeled as spheres, where intercalated lithium undergoes isotropic linear diffusion [47, 48]. For phase separating materials, such as Li_xFePO_4 (LFP), each particle is assumed to have a spherical phase boundary that moves as a "shrinking core", as one phase displaces the other [43, 110, 116]. In these models, the local Nernst equilibrium potential is fitted to the global open circuit voltage of the cell, but this neglects nonuniform composition, which makes the voltage plateau an emergent property of the porous electrode [5, 42, 49, 50]. For thermodynamic consistency, all of these phenomena should derive from common thermodynamic principles and cannot be independently fitted to experimental data. The open circuit voltage reflects the activity of intercalated ions, which in turn affects ion transport in the solid phase and Faradaic reactions involving ions in the electrolyte phase [10, 11].

In this paper, we extend porous electrode theory to non-ideal active materials, including those capable of phase transformations. Our starting point is a general phase-field theory of ion intercalation kinetics developed by our group over the past five years [5, 11, 14, 30, 31, 108], which has recently led to a quantitative understanding of phase separation dynamics in LFP nanoparticles [42]. The ionic fluxes in all phases are related to electrochemical potential gradients, consistent with non-equilibrium thermodynamics [7, 57]. This approach has been used extensively in recent years to model transport in electrochemical systems [15, 19, 69, 74, 75, 83–86, 96] and nonlinear electrokinetic phenomena [13, 14, 18, 111]. For thermodynamic consistency,

we also relate the Faradaic reaction rate to electrochemical potential differences between the oxidized, reduced, and transition states, leading to a generalized Butler-Volmer equation [5, 11, 42] suitable for phase-separating materials. These elements are integrated in a general porous electrode theory, where the active material is described by a Cahn-Hilliard phase-field model [7, 92], as in nanoscale simulations of Li-ion battery materials [5, 30, 31, 42, 56, 61, 71, 108, 113]. This allows us to describe the non-equilibrium thermodynamics of porous battery electrodes in terms of well established physical principles for ion intercalation in nanoparticles.

II. BRIEF HISTORY OF POROUS ELECTRODE THEORY

We begin by reviewing volume-averaged porous electrode theory, which has been the standard approach in battery modeling for the past 50 years. The earliest papers dealing with porous electrode theory were published in the late 1950's and early 1960's, by Ksenzhek and Stender [78–80] and Euler and Nonnenmacher [52]. This work treated current density distributions in porous electrodes, which were characterized by volume averaged properties, such as porosity, average surface area per volume, and conductivity.

A few years later, Newman and Tobias expanded the analysis to account for the effects of concentration variations on kinetics with concentration independent electrolyte properties. [95] This paper also introduced the well known equation for mass conservation inside a porous electrode undergoing reactions. Around the same time, de Levie published his work modeling diffusion inside pores, capacitance effects, and combined effects of double layer capacitance, diffusion, and kinetics. [44, 45] These models included linear capacitance effects for the double layer and utilized equivalent circuit models for the porous electrode.

Another notable paper is by Ksenzhek, which incorporated concentrated solution theory in the transport equations inside a porous electrode, and referred to gradients in electrochemical potential as the driving force for transport. [77] (for more on force and flux coupling, refer to [7]) Ksenzhek's paper introduced many of the same concepts used in this paper to treat transport processes in the electrode. Much of the earlier work on modeling porous electrodes relied on deriving the volume averaged governing equations as well as some analytical results for small overpotential (i.e. linearized) or high overpotential (i.e. Tafel) regime kinetics. [67] Other notable papers include modeling transport effects in steady state operation [58] and transient behavior of a porous electrode subjected to galvanostatic discharge with sinusoidal perturbations. [103]

Many of the volume averaged principles have underlying assumptions regarding properties of the cell that can be critical to performance. The validity of these assumptions was reviewed by Grens. [66] It was found that the assumption of constant conductivity can be used over a wide range of operating conditions. The assumption of constant electrolyte concentration, which was used to simplify systems in early papers, is only valid over a narrow range of operating conditions, as is expected.

In 1975, Newman and Tiedemann published a review of porous electrode theory. [94] This paper summarized mass and charge conservation equations and kinetic equations for batteries and other types of electrochemical systems. A few years later, Atlung *et al.* investigated the dynamics of solid solution (i.e. intercalation) electrodes for different time scales with respect to the limiting current. [4] Pollard and Newman investigated the transient behavior of porous electrodes at high exchange current densities (i.e. small overpotential). [100] These two papers appear to be some of the earliest studies of the time dependence of porous electrode systems. Up to this point, the literature was predominantly based on linearized Butler-Volmer and exponential Tafel kinetics, due to limited computational power.

As computers and numerical methods advanced, so did simulations of porous electrodes. West *et al.* demonstrated the use of numerical methods to simulate discharge of a porous TiS_2 electrode (without the separator), and how the main limiting factor is the depletion of the electrolyte. [122] This is one of the earliest demonstrations of solving the porous electrode equations using numerical methods. About ten years later, Doyle, Fuller and Newman modeled a separator and porous electrode under constant current disharge. [47] This paper was one of the first to model the reaction rate with the Butler-Volmer equation, instead of linearized kinetics or a Tafel equation. The next year, Fuller, Doyle and Newman published a similar model of a dual lithium-ion insertion cell (graphite anode and manganese oxide cathode) [54]. Doyle et al. then published a comparison of model predictions with experimental data for the full lithium-ion battery (anode and cathode) [48] These papers are of great importance in the field, as they developed the first complete simulations of lithium-ion batteries and solidified the role of porous electrode theory in modeling these systems. The same theoretical framework has been applied to many other types of cells, such as lithium-sulfur [81] and LFP [43, 110] batteries.

Battery models invariably assume electroneutrality, but diffuse charge in porous electrodes has received increasing attention over the past decade, driven by applications in energy storage and desalination. The effects of double-layer capacitance in a porous electrode were originally considered using only linearized low-voltage models [70, 118], which are equivalent to transmission line circuits [44, 45, 51]. Recently, the full nonlinear dynamics of capacitive charging and salt depletion have been analyzed and simulated in both flat [16, 96] and porous [20] electrodes. The combined effects of electrostatic capacitance and pseudo-capacitance due to Faradaic reactions have also been incorporated in porous

electrode theory [21, 22], using Frumkin-Butler-Volmer kinetics [12, 17, 28, 68, 76]. These models have been successfully used to predict the nonlinear dynamics of capacitive desalination by porous carbon electrodes [23, 101].

Computational and experimental advances have also been made to study porous electrodes at the microstructural level and thus test the formal volume-averaging, which underlies macroscopic continuum models. Garcia et al. performed finite-element simulations of ion transport in typical porous microstructures for Li-ion batteries [56], and Garcia and Chang simulated hypothetical inter-penetrating 3D battery architectures at the particle level [55]. Recently, Smith, Garcia and Horn analyzed the effects of microstructure on battery performance for various sizes and shapes of particles in a $Li_{1-x}C_6/Li_xCoO_2$ cell [109]. The study used 3D image reconstruction of a real battery microstructure by focused ion beam milling, which has led to detailed studies of microstructural effects in porous electrodes [73, 115, 117]. In this paper, we will discuss mathematical bounds on effective diffusivities in porous media, which could be compared to results for actual battery microstructures. Recently, it has also become possible to observe lithium ion transport at the scale in individual particles in porous Li-ion battery electrodes [6, 121], which could be invaluable in testing the dynamical predictions of new mathematical models.

III. PHASE SEPARATING ELECTRODES

A. Lithium Iron Phosphate

The discovery of LFP as a cathode material by the Goodenough group in 1997 has had a large and unexpected impact on the battery field, which provides the motivation for our work. LFP was first thought to be a low-power material, and it demonstrated poor capacity at room temperature. [98] The capacity has since been improved via conductive coatings and the formation of nanoparticles. [64, 104], and the rate capability has been improved in similar ways [63, 87]. With high carbon loading to circumvent electronic conductivity limitations, LFP nanoparticles can now be discharged in 10 seconds [71]. Off-stochiometric phosphate glass coatings contribute to this high rate, not only in LFP, but also in $LiCoO_2$ [112].

It has been known since its discovery that LFP is a phase separating material, as evidenced by a flat voltage plateau in the open circuit voltage [98, 114]. There are a wide variety of battery materials with multiple stable phases at different states of charge [65], but Li_xFePO_4 has a particularly strong tendency for phase separation, with a miscibility gap (voltage plateau) spanning across most of the range from $x = 0$ to $x = 1$ at room temperature. Padhi et al. first depicted phase separation inside LFP particles schematically as a "shrinking core" of one phase being replaced by an outer shell of the other phase during charge/discharge cycles [98]. Srinivasan and Newman encoded this concept in a porous electrode theory of the LFP cathode with spherical active particles, containing spherical shrinking cores. [110] Recently, Dargaville and Farrell have expanded this approach to predict active material utilization in LFP electrodes. [43] Thorat *et al.* have also used the model to gain insight into rate-limiting mechanisms inside LFP cathodes. [116]

To date, the shrinking-core porous electrode model is the only model to successfully fit the galvanostatic discharge of an LFP electrode, but the results are not fully satisfactory. Besides neglecting the microscopic physics of phase separation, the model relies on fitting a concentration-dependent solid diffusivity, whose inferred values are orders of magnitude smaller than *ab initio* simulations [87, 91] or impedance measurements [99]. More consistent values of the solid diffusivity have since been obtained by different models attempting to account for anisotropic phase separation with elastic coherency strain. [123] Most troubling for the shrinking core picture, however, is the direct observation of phase boundaries with very different orientations. In 2006, Chen and Richardson published images showing the orientation of the phase interface aligned with iron phosphate planes and reaching the active facet of the particle. [40] This observation was supported by experiments of Delmas *et al.*, who suggested a "domino-cascade model" for the intercalation process inside LFP [46]. With further experimental evidence for anisotropic phase morphologies [97, 121], it has become clear that a new approach is needed to capture the non-equilibrium thermodynamics of this material.

B. Phase-Field Models

Phase-field models are widely used to describe phase transformations and microstructural evolution in materials science [7, 41], but they are relatively new to electrochemistry. In 2004, Guyer, Boettinger, Warren and McFadden [59, 60] first modeled the sharp electrode/electrolyte interface with a continuous phase field varying between stable values 0 and 1, representing the liquid electrolyte and solid metal phases. As in phase-field models of dendritic solidification [25–27, 72], they used a simple quartic function to model a double-welled homogeneous free energy. They described the kinetics of electrodeposition [60] (converting ions in the electrolyte to solid metal) by Allen-Cahn-type kinetics [2, 41], linear in the thermodynamic driving force, but did not make connections with the Butler-Volmer equation. Several groups have used this approach to model dendritic electrodeposition and related processes [1, 3, 106]. Also in 2004, Han, Van der Ven and Ceder [61] first applied the Cahn-Hilliard equation[7, 32–34, 37, 41] to the diffusion of intercalated lithium ions in LFP, albeit without modeling reaction kinetics.

Building on these advances, Bazant developed a general theory of charge-transfer and Faradaic reaction ki-

netics in concentrated solutions and solids [9–11], suitable for use with phase-field models. The exponential Tafel dependence of the current on the overpotential, defined in terms of the variational chemical potentials, was first reported in 2007 by Singh, Ceder and Bazant [107, 108], but with spurious pre-factor, corrected by Burch [29, 30]. The model was used to predict "intercalation waves" in small, reaction-limited LFP nanoparticles in 1D [108], 2D [31], and 3D [113], thus providing a mathematical description of the domino cascade phenomenon [46]. The complete electrochemical phase-field theory, combining the Cahn-Hilliard with Butler-Volmer kinetics and the cell voltage, appeared in 2009 lectures notes [9, 10] and was applied to LFP nanoparticles [5, 42].

The new theory has led to a quantitative understanding of intercalation dynamics in single nanoparticles of LFP. Bai, Cogswell and Bazant [5] generalized the Butler-Volmer equation using variational chemical potentials (as derived in the supporting information) and used it to develop a mathematical theory of the suppression of phase separation in LFP nanoparticles with increasing current. This phenomenon, which helps to explain the remarkable performance of nano-LFP, was also suggested by Malik and Ceder based on bulk free energy calculations [88], but the theory shows that it is entirely controlled by Faradaic reactions at the particle surface [5, 42]. Cogswell and Bazant [42] have shown that including elastic coherency strain in the model leads to a quantitative theory of phase morphology and lithium solubility. Experimental data for different particles sizes and temperatures can be fitted with only two parameters (the gradient penalty and regular solution parameter, defined below).

The goal of the present work is to combine the phase-field theory of ion intercalation in nanoparticles with classical porous electrode theory to arrive at a general mathematical framework for non-equilibrium thermodynamics of porous electrodes. Our work was first presented at the Fall Meeting of the Materials Research Society in 2010 and again at the Electrochemical Society Meetings in Montreal and Boston in 2011. Around the same time, Lai and Ciucci were thinking along similar lines [83, 85] and published an important reformulation of Newman's porous electrode theory based non-equilibrium thermodynamics [86], but they did not make any connections with phase-field models or phase transformations at the macroscopic electrode scale. (Their treatment of reactions also differs from Bazant's theory based on generalized Butler-Volmer kinetics [9–11].)

In this paper, we develop a variational thermodynamic description of electrolyte transport, electron transport, electrochemical kinetics, and phase separation, and we apply to Li-ion batteries in what appears to be the first mathematical theory and computer simulations of *macroscopic phase transformations in porous electrodes*. Simulations of discharge into a cathode consisting of multiple phase-separating particles interacting via an electrolyte reservoir at constant chemical potential were reported by Burch [29], who observed "mosaic instabilities", where particles transform one-by-one at low current. This phenomenon was elegantly described by Dreyer et al. in terms of a (theoretical and experimental) balloon model, which helps to explain the noisy voltage plateau and zero-current voltage gap in slow charge/discharge cycles of porous LFP electrodes [49, 50]. These studies, however, did not account for electrolyte transport and associated macroscopic gradients in porous electrodes undergoing phase transformations, which are the subject of this work. To do this, we must reformulate Faradaic reaction kinetics for concentrated solutions, consistent with the Cahn-Hilliard equation for ion intercalation and Newman's porous electrode theory for the electrolyte.

IV. GENERAL THEORY OF REACTIONS AND TRANSPORT IN CONCENTRATED SOLUTIONS

In this section, we begin with a general theory of reaction rates based on non-equilibrium thermodynamics and transition state theory. We then expand the model to treat transport in concentrated solutions (i.e. solids). Finally, we show that this concentrated solution model collapses to Fickian diffusion in the dilute limit.

A. General Theory of Reaction Rates

Consider a single step reaction consisting of two states, State 1 and State 2, which proceeds through some transition state. Figure 1 gives an energy landscape for this reaction.

The transition state is assumed to be short lived and each species that reaches the transition state reacts (i.e. continues through the transition state) with a probability of one. This reaction can be represented via the following.

$$\text{State 1} \rightleftharpoons \text{Transition State} \rightleftharpoons \text{State 2}$$

Thermal fluctuations cause particles to undergo rapid changes in energy. These changes in energy, while random, can be represented by some statistical distribution of energy states. This distribution, known as the Boltzmann distribution, gives the percentage of particles with a given energy relative to their local equilibrium state. This energy difference is expressed as a free energy difference per particle, which is also referred to as a chemical potential. To develop a model for the reaction rate in each direction, we start with an attempt frequency, which gives the number of reaction attemps per second, and then multiply this by the probability (i.e. fraction of total particles) that a particle has enough energy to reach the transition state. The forward and reverse reaction rates are

$$R_{\rightarrow} = R_{o,f} \exp\left(-\frac{\mu_{\ddagger} - \mu_1}{k_B T}\right) \tag{1}$$

and

$$R_{\leftarrow} = R_{o,r} \exp\left(-\frac{\mu_{\ddagger} - \mu_2}{k_B T}\right). \tag{2}$$

The terms $R_{o,f}$ and $R_{o,r}$ represent the reaction attempts for the forward and reverse reactions, respectively, while the exponential term is the probability that a particle has enough energy to reach the reaction rate. Here it is assumed that once the particle reaches the transition state, the probability that it proceeds is one. Another way to interpret the $R_{o,f}$ and $R_{o,r}$ terms is as the "barrier-less" reaction rate for the reactions. That is, the rate when the activation energy goes to zero. Typically, for systems with no temperature gradients or external energy sources (e.g. electromagnetic), $R_{o,f} = R_{o,r}$. The net reaction rate of a particle traveling from State 1 to State 2 is given by the difference between the forward and backwards reaction rates. Furthermore, for a given temperature, the number of particles in a system at the transition state is essentially constant. This allows the ideal component of the chemical potential to be absorbed into the constant. This yields the net reaction rate,

$$R_{1\rightarrow 2} = R_o \left[\exp\left(-\frac{\mu_{\ddagger}^{ex} - \mu_1}{k_B T}\right) - \exp\left(-\frac{\mu_{\ddagger}^{ex} - \mu_2}{k_B T}\right)\right]. \tag{3}$$

This reaction rate is very general, and can be used to model any activated reaction that occurs at constant temperature, where the excess chemical potential barriers are much larger than the thermal voltage $k_B T/e$. Next, this reaction rate model will be used to derive a model for transport in concentrated solutions. Later, this reaction rate expression will be adopted to form the Butler-Volmer Equation.

B. General Theory of Transport in Solids and Concentrated Solutions

Transport in solids and concentrated solutions can also be treated as reactions. Particles begin in one energy state, and move through some transition state to a different energy state. In the case of transport, though, the energy state is related to the particle's environment (i.e. surroundings). Figure 2 demonstrates this concept and shows an energy landscape for a particle moving through a medium.

Diffusion consists of thermally activated jumps over some distance between sites. Let's consider the average time between these transitions, τ. We know that τ should approach some limit as the energy barrier between sites approaches zero. Let's refer to this value as τ_o, which τ should collapse to in the barrier-less limit. Similarly to how reactions proceed, we need to consider the probability that a particle has enough energy to overcome the energy barrier and reach the transition state. The mean time between transitions should be inversely proportional to the probability that a particle has enough energy to reach the transition state. The constant of proportionality can be absorbed into the constant τ_o.

$$\tau = \frac{\tau_o}{\exp\left(-\frac{\mu_{\ddagger}^{ex} - \mu^{ex}}{k_B T}\right)} \tag{4}$$

The diffusivity, D is defined as the average jump distance squared divided by the average time between jumps. Using this definition, the diffusivity is

$$D = \frac{(\Delta x)^2}{\tau} = \frac{(\Delta x)^2}{\tau_o}\left(\frac{\gamma}{\gamma_{\ddagger}}\right) = D_o\left(\frac{\gamma}{\gamma_{\ddagger}}\right). \tag{5}$$

1. *Diffusivity of an Ideal Solid Solution*

To model an ideal solid solution, a lattice gas model is used, which accounts for finite volume effects in the medium and treats the particles as hard spheres. Figure 3 illustrates this model.

For an ideal solid solution, we can neglect particle-particle interactons. The chemical potential for a particle in an ideal solid solution is

$$\mu = k_B T \ln\left(\frac{\tilde{c}}{1-\tilde{c}}\right) + \mu^o, \tag{6}$$

where μ^o is the chemical potential of the reference state. For a particle, each other particle occupies one available site. However, the transition state requires two available sites, effectively doubling the excluded volume contribution to the chemical potential. Using the definition of the activity coefficient, $\mu = k_B T \ln a = k_B T \ln(c\gamma)$, we obtain the activity coefficients of the particle in the site, and in the activated state,

$$\gamma = \left(1 - \frac{c}{c_{max}}\right)^{-1} \exp\left(-\frac{\mu_{min}}{k_B T}\right), \tag{7}$$

$$\gamma_{\ddagger} = \left(1 - \frac{c}{c_{max}}\right)^{-2} \exp\left(-\frac{\mu_{\ddagger}}{k_B T}\right). \tag{8}$$

Inserting these two activity coefficients into Equation 5, the diffusivity, D, is

$$D = D_o\left(1 - \frac{c}{c_{max}}\right). \tag{9}$$

This diffusivity is for an ideal solid solution with a finite number of lattice sites available for particles. As the lattice sites fill, the diffusivity of a particle goes to zero, since the particle is unable to move as it is blocked by other particles on the lattice.

2. *Concentrated Solution Theory Derivation*

Here we will derive the general form of concentrated solution theory, which predicts that the flux can be modeled as

$$\mathbf{F} = -Mc\nabla\mu, \tag{10}$$

where M is the mobility. Let's consider the scenario in Figure 3, where a particle is sitting in an energy well. This particle's energy fluctuates on the order of k_BT until it has enough energy to overcome some energy barrier that exists between the two states. Figure 4 demonstrates this in one dimension. The flux, $\mathbf{F}$, is

$$\mathbf{F}_i = \frac{R}{A}\mathbf{e}_i, \tag{11}$$

where $\mathbf{e}_i$ is a coordinate vector in the i direction and $\mathbf{F}_i$ is the flux in the i direction.

We see that the particle's chemical potential is a function of location, as concentrations and therefore chemical potentials, will vary with position. First, we begin with Equation (4). Let's define the right side of the page as the positive x-direction. Using our previous defined form of the reaction rate in Equation (3), we can substitute this into Equation (11). However, we need an expression for the barrierless reaction rate. This comes from the barrierless diffusion time in Equation (4). The barrierliess reaction rate should be equivalent to the inverse of two times the barrierless diffusion time. The one half comes from the probability the particle travels in the positive x direction.

$$R_o = \frac{1}{2\tau_o} \tag{12}$$

Plugging this into Equation (11) along with Equation (3), and considering the fact that our chemical potential is a function of position, we obtain

$$\mathbf{F}_x = \frac{1}{2\tau_o A_{cell}\gamma_\ddagger}\left[\exp\left(\tilde{\mu}(x) - \frac{\Delta x}{2}\frac{\partial\tilde{\mu}(x)}{\partial x}\right) - \exp\left(\tilde{\mu}(x) + \frac{\Delta x}{2}\frac{\partial\tilde{\mu}(x)}{\partial x}\right)\right], \tag{13}$$

where $\tilde{\mu}(x)$ denotes the chemical potential scaled by the thermal voltage, k_BT. Next, we assume that the particle is close to equilibrium. That is, the difference in chemical potential between the states is small. This allows us to linearize Equation (13). Linearizing the equation yields

$$\mathbf{F}_x = -\frac{a(x)}{\tau_o A\gamma_\ddagger}\left(\frac{\Delta x}{2}\right)\frac{\partial\tilde{\mu}(x)}{\partial x}, \tag{14}$$

where $a(x)$ is the activity as a function of position. This can be simplified to $a(x) = V\gamma(x)c(x)$. Plugging this into Equation (14), using our definition of the diffusivity, D, from Equation (5), and the Einstein relation, which states that $M = D/k_BT$, we obtain the flux as predicted by concentrated solution theory in the x dimension. We can easily expand this to other dimensions. Doing so, we obtain the form of the flux proposed by concentrated solution theory,

$$\mathbf{F} = -Mc\nabla\mu, \tag{15}$$

where $c = c(x, y, z)$. Taking the dilute limit, as $c \to 0$, and using the definition of chemical potential, $\mu = k_BT\ln a$, where $a = \gamma c$ and $\gamma = 1$ (dilute limit), we obtain Fick's Law from Equation (15),

$$\mathbf{F} = -D\nabla c. \tag{16}$$

V. CHARACTERIZATION OF POROUS MEDIA

In lithium-ion batteries, the electrodes are typically composites consisting of active material (e.g. graphite in the anode, iron phosphate in the cathode), conducting material (e.g. carbon black), and binder. The electrolyte penetrates the pores of this solid matrix. This porous electrode is advantageous because it substantially increases the available active area of the electrode. However, this type of system, which can have variations in porosity (i.e. volume of electrolyte per volume of the electrode) and loading percent of active material throughout the volume, presents difficulty in modeling. To account for the variation in electrode properties, various volume averaging methods for the electrical conductivity and transport properties in the electrode are employed. In this section, we will give a brief overview of modeling the conductivity and transport of a heterogeneous material, consisting of two or more materials with different properties. The conductvitiy bounds in this section include the Wiener bounds, Hashin-Shtrikman bounds, percolation theory, and the Bruggeman empirical relation. [10, 90, 105, 119]

A. Electrical Conductivity of the Porous Media

To characterize the electrical conductivity of the porous media, we will consider upper and lower bounds for anisotropic and isotropic media. First we consider an anisotropic material as shown in Figure 5.

The left image in Figure 5 represents the different materials in parallel. This produces the lowest resistance, and represents the upper limit of the conductivity of the heterogeneous material. The right image represents the materials in series, which produces the lower limit of the conductivity (i.e. highest effective resistance). These limits are referred to as the upper and lower Wiener bounds, respectively. Let Φ_i be the volume fraction of material i. For the upper Wiener bound, the equivalent circuit is resistors in parallel. The effective conductivity for this system is

$$\overline{\sigma}_{max} = \langle\sigma\rangle = \sum_i \Phi_i\sigma_i. \tag{17}$$

The lower Wiener bound can be represented by resistors in series. For this equivalent circuit, an effective conductivity is

$$\overline{\sigma}_{min} = \langle\sigma^{-1}\rangle^{-1} = \frac{1}{\sum_i \frac{\Phi_i}{\sigma_i}}. \tag{18}$$

For an anisotropic material, the effective conductivity, $\overline{\sigma}$, must lie within the Wiener bounds,

$$\langle \sigma^{-1} \rangle^{-1} \leq \overline{\sigma} \leq \langle \sigma \rangle. \tag{19}$$

Next, we consider an isotropic material consisting of two different materials. The Hashin-Shtrikman bounds for an isotropic material in d dimensions gives the bounds for the macroscopic conductivity. The bounds are calculated by creating concentric circles of varying size with equal volume fractions of two materials of different conductivities. The spheres are in contact, and maximum conductivity is achieved when $\sigma_1 > \sigma_2$, as this provides the highest conductivity pathway. The minimum conductivity corresponds to the case where $\sigma_2 > \sigma_1$, then the only complete pathway is through the material of lower conductivity. Any combination should lie within these limits for constant conductivities. Figure 6 depicts the isotropic material.

For the case where $\sigma_1 > \sigma_2$, the Hashin-Shtrikman bounds for an isotropic two-component material in d dimensions is

$$\langle \sigma \rangle - \frac{(\sigma_1 - \sigma_2)^2 \Phi_1 \Phi_2}{\langle \tilde{\sigma} \rangle + \sigma_2 (d-1)} \leq \overline{\sigma} \leq \langle \sigma \rangle - \frac{(\sigma_1 - \sigma_2)^2 \Phi_1 \Phi_2}{\langle \tilde{\sigma} \rangle + \sigma_1 (d-1)}, \tag{20}$$

where

$$\langle \sigma \rangle = \Phi_1 \sigma_1 + \Phi_2 \sigma_2$$

and

$$\langle \tilde{\sigma} \rangle = \Phi_1 \sigma_2 + \Phi_2 \sigma_1.$$

The Wiener and Hashin-Shtrikman bounds provide us with suitable ranges for isotropic and anisotropic media with two components. For the case of a porous electrode, the Hashin-Shtrikman bounds are reasonable for electron conduction, since the solid electron conducting matrix typically consists of a solid with high conductivity, permeated by an electrolyte of very low conductivity. Figure 7 gives the Wiener and Hashin-Shtrikman bounds for two materials, with conductivities of 1.0 and 0.1.

Next, we consider ion transport in porous media. Ion transport in porous media often consists of a solid phase, which has little to no ionic conductivity (i.e. slow or no diffusion) permeated by an electrolyte phase which has very high ionic conductivity (i.e. fast diffusion). In the next section, we will compare different models for effective porous media properties.

B. Transport in Porous Media

For the case of ion transport in porous media, there is an electrolyte phase, which has a non-zero diffusivity, and the solid phase, through which transport is very slow (essentially zero compared to the electrolyte diffusivity). Here, we consider the pores (electrolyte phase) and give the solid matrix a zero conductivity. The volume fraction of phase 1 (the pores), Φ_1, is the porosity of the media. That is

$$\Phi_1 = \epsilon_p,\ \sigma_1 = \sigma_p.$$

The conductivity for all other phases is zero. This reduces the Wiener (anisotropic) and Hashin-Shtrikman (isotropic) lower bounds to zero. If we assume the media consists of two phases ($\Phi_2 = 1 - \epsilon_p$, $\sigma_2 = 0$), then the Wiener and Hashin-Shtrikman upper bounds can be simplified to

$$\overline{\sigma}_{max}^{Wiener} = \Phi_1 \sigma_1 = \epsilon_p \sigma_p, \text{ and} \tag{21}$$

$$\overline{\sigma}_{max}^{HS} = \sigma_p \epsilon_p \left(\frac{d-1}{d - \epsilon_p} \right). \tag{22}$$

In Equation (22), d is the dimensionality. This section will also compare two other typically used models. The percolation model, which assumes isotropic media, has a zero conductivity below some critical porosity. Above the critical porosity, the conductivity approaches its maximum quickly. The critical porosity is the porosity at which a pathway across the media is attained. The effective conductivity, using the percolation model for some critical porosity, ϵ_c, is given by

$$\overline{\sigma}_{perc} \sim (\epsilon_p - \epsilon_c)^t. \tag{23}$$

Just above the critical porosity, ϵ_c, the exponent $t = 2$ is typically used in three dimensions. This behavior is captured by

$$\overline{\sigma}_{perc} \cong \begin{cases} \sigma_p \left(\frac{\epsilon_p - \epsilon_c}{1 - \epsilon_c} \right)^2 & \epsilon_c \leq \epsilon_p \leq 1 \\ 0 & 0 \leq \epsilon_p \leq \epsilon_c \end{cases}. \tag{24}$$

Finally, we consider the Bruggeman formula, an empirical model which is predominantly used in electrochemistry,

$$\overline{\sigma}_B = \epsilon_p^{3/2} \sigma_p. \tag{25}$$

Using these relations for the conductivity, we next relate this conductivity to the effective diffusivity for some volume of a porous medium. Figure (9) demonstrates a typical volume of porous media.

The porosity is the volume of the electrolyte as a fraction of the total volume. If the porosity is assumed to be constant throughout the volume, then the area of each face of the volume is proportional to the porosity. Also, the total mass inside the volume is given by the volume averaged concentration, $\overline{c} = \epsilon_p c$. We begin with a mass balance on the volume,

$$\frac{\partial \overline{c}}{\partial t} + \nabla \cdot \mathbf{F} = 0, \tag{26}$$

where $\mathbf{F}$ is the flux at the surfaces of the volume. The net flux is

$$\mathbf{F} = -\overline{\sigma}_d \nabla c, \tag{27}$$

where c is the concentration in the pores. Regardless of porosity fluctuations in space, at equilibrium the concentration is constant throughout the volume. This is because equilibrium depends on chemical potential. Combining Equations (26) and (27), we get

$$\frac{\partial c}{\partial t} = \overline{D}\nabla^2 c, \tag{28}$$

where the effective diffusivity in a porous medium, $\overline{D}$, is given by

$$\overline{D} = \frac{\overline{\sigma}_p}{\epsilon_p}.$$

The reduction of the diffusivity inside a porous medium can be interpreted as a reduction of the mean free path. The factor by which this characteristic length is changed is defined as the tortuosity, τ_p. In a porous material, for some free solution characteristic length, L, the porous characteristic length is

$$L_p = \tau_p L. \tag{29}$$

Given that $D \sim L^2/t_d$, the tortuosity scales the characteristic length, L,

$$\overline{D} = \frac{D_p}{\tau_p^2}. \tag{30}$$

Combining this with the above relation between the conductivity and effective diffusivity, the effective conductivity can be expressed as

$$\overline{\sigma}_d = \frac{D_p \epsilon_p}{\tau_p^2}. \tag{31}$$

Using this relation, along with the conductivities for each model in the previous section, the tortuosity relation to the porosity can be derived. Given that the conductivities shown were the upper bounds for the Wiener and Hashin-Shtrikman models, the calculated tortuosity values represent the lower bounds (conductivity is inversely proportional to the square of the tortuosity). The Wiener lower bound tortuosity for anisotropic pores is

$$\tau_p^{Wiener} = 1. \tag{32}$$

For the Hashin-Shtrikman model, the lower bound of the tortuosity is

$$\tau_p^{HS} = \sqrt{\left(\frac{d-\epsilon_p}{d-1}\right)} \tag{33}$$

in d dimensions. The percolation model produces a piecewise function for the tortuosity, above and below the critical porosity, which is given by

$$\tau_p^{perc} \cong \begin{cases} \sqrt{\epsilon_p}\left(\frac{1-\epsilon_c}{\epsilon_p-\epsilon_c}\right) & \epsilon_c \le \epsilon_p \le 1 \\ \infty & 0 \le \epsilon_p \le \epsilon_c \end{cases} \tag{34}$$

As the conductivity approaches zero, the tortuosity makes no physical sense as it no longer represents the extra path length. Instead it represents the decreasing number of available percolating paths, which are the cause of the lowered conductivity. Finally, from the Bruggeman empirical relation we get the empirical tortuosity,

$$\tau_p^B = \epsilon^{-1/4}. \tag{35}$$

This section represents the most typical models used to determine effective properties of porous media. The Hashin-Shtrikman bounds for the effective conductivity represent appropriate limits for typical porous media. Porous media does not often demonstrate anisotropic behavior. Furthermore, a lithium-ion battery typically consists of two phases: a solid phase (with its own effective conductivity), and an electrolyte phase. Typically, the Bruggeman empirical model, which lies within these limits, is used. [47, 54, 110]

VI. POROUS ELECTRODE THEORY

A. Conservation Equations

Using the principles laid out in the first section of this paper on concentrated solution theory, the Porous Electrode Theory equations will be derived using mass and charge conservation combined with the Nernst-Planck Equation and a modified form of the Butler-Volmer Equation. The derivation will present the equations and how their properties have deep ties to the thermodynamics of the system. Then, the equations will be nondimensionalized and scaled appropriately using characteristic time and length scales in the system.

1. Mass and Charge Conservation

We begin with the definition of flux based on concentrated solution theory. Assuming the system is close to equilibrium, the mass flux is

$$\mathbf{N}_i = -M_i c_i \nabla \mu_i, \tag{36}$$

where M_i is the mobility of species i, c_i is the concentration of species i, and μ_i is the chemical potential of species i. The conservation equation for concentration is given by the divergence of the flux,

$$\frac{\partial c_i}{\partial t} = -\nabla \cdot \mathbf{N}_i - R_i. \tag{37}$$

In order to express this conservation equation in a form that is relevant to electrochemical systems, we must first postulate a suitable form of the chemical potential. We begin with the standard definition of the chemical potential including the activity contribution, then include

electrostatic effects to obtain

$$\mu_i = k_B T \ln(a_i) + z_i e \phi. \tag{38}$$

This chemical potential can be inserted into Equation (36). If the activity of the electrolyte is available from experimental values, then this form of the flux facilitates its use. However, diffusivities are typically given as a function of concentration. Simplifying Equation (36) using Equation (38) for the chemical potential yields the Nernst-Planck Equation,

$$\mathbf{N}_i = -D_i \left(1 + \frac{\partial \ln \gamma_i}{\partial \ln c_i}\right) \nabla c_i - \frac{e z_i}{k_B T} D_i c_i \nabla \phi, \tag{39}$$

where D_i is the diffusivity of species i (which can also be concentration dependent), γ_i is the activity coefficient, and ϕ is the potential.

For the bulk electrolyte, the electroneutrality approximation will be used. This approximation assumes that the double layers are thin, which is a reasonable approximation for the typical concentrations of the electrolyte. (For porous electrode modeling including double layer effects, see Refs. [20–22].) The electroneutrality approximation assumes

$$\rho = z_+ c_+ - z_- c_- \approx 0, \tag{40}$$

where z_+ and z_- are defined as the absolute values of the charge of the cation and anion, respectively. Next, it is assumed that the electrolye is a binary electrolyte, consisting of a single positive species (i.e. Li^+) and a single negative species (e.g. PF_6^-).

For porous electrodes, we also need to account for the porosity of the medium. The porosity affects the interfacial area between volumes of the porous electrode. It also affects the concentration of a given volume of the electrode. Accounting for porosity, Equations (37) and (36) become

$$\epsilon \frac{\partial c_i}{\partial t} = -\nabla \cdot \mathbf{N}_i - R_i, \text{ and} \tag{41}$$

$$\mathbf{N}_i = -\epsilon M_i c_i \nabla \mu_i, \tag{42}$$

where ϵ is the porosity, which is the volume of electrolyte per volume of the electrode. This value may change with position, but this derivation assumes porosity is constant with respect to time. With this assumption, the Nernst-Planck Equation can be defined for the positive and negative species in the electrolyte. This yields the cation and anion fluxes,

$$\mathbf{N}_+ = -\epsilon D_+ \nabla c_+ - \epsilon \frac{z_+ e}{k_B T} D_+ c_+ \nabla \phi, \text{ and} \tag{43}$$

$$\mathbf{N}_- = -\epsilon D_- \nabla c_- + \epsilon \frac{z_- e}{k_B T} D_- c_- \nabla \phi. \tag{44}$$

Next, the flux equations for the cation and anion in Equations (43) and (44) are inserted into Equation (41) and combined with the electroneutrality assumption in Equation (40) to eliminate the potential. If it is assumed that the anion does not react (which is reasonable if the SEI is not modeled), the mass conservation equation is

$$\epsilon \frac{\partial c}{\partial t} = \nabla \cdot (\epsilon D_{amb} \nabla c) - \nabla \cdot \left(\left(\frac{t_+ - t_-}{2} \right) \mathbf{i} \right) - \frac{z_+ R_+}{2}, \tag{45}$$

where t_+ and t_- are the cation and anion transference numbers, respectively, and D_{amb} is the ambipolar diffusivity. These values are defined as

$$t_\pm \equiv \frac{z_\pm D_\pm}{z_+ D_+ + z_- D_-}, \text{ and} \tag{46}$$

$$D_{amb} \equiv \frac{D_+ D_- (z_+ + z_-)}{z_+ D_+ + z_- D_-}. \tag{47}$$

In equation (45), $\mathbf{i}$ is the current density in the electrolyte, which is given by the sum of the cation and anion fluxes multiplied by their charge,

$$\mathbf{i} = e z_+ \mathbf{N}_+ - e z_- \mathbf{N}_-. \tag{48}$$

Furthermore, the concentration c, using the electroneutrality assumption, is defined as

$$c \equiv z_+ c_+ = z_- c_-. \tag{49}$$

Next, it is necessary to relate the charge conservation to the mass conservation to simplify Equation (45).

The electroneutrality approximation puts a restriction on the charge accumulation in the electrolyte. Given that the total number of anions in the electrolyte is fixed, and that the anion is neither consumed nor produced in the system (i.e. $R_- = 0$), then the number of cations that enter a volume, minus those that leave, must equal the number produced or consumed by the reactions in that volume. To determine the charge balance in some volume of the electrode, we begin with the current density as given by Equation (48). Simplifying this expression and combining it with the definition of c based on the electroneutrality assumption, the current density is

$$\mathbf{i} = -e (D_+ - D_-) \epsilon \nabla c - \frac{e^2}{k_B T} (z_+ D_+ + z_- D_-) \epsilon c \nabla \phi. \tag{50}$$

The divergence of the current density gives the accumulation of charge within a given volume. As stated above, this value must equal the charge produced or consumed by the reactions within the given volume, therefore

$$e z_+ R_+ = e a_p j_{in} = -\nabla \cdot \mathbf{i}, \tag{51}$$

where a_p is the area per unit volume of the particles and j_{in} is the flux into the particles due to Faradaic reactions. Substituting this expression into Equation (45) and using the definition $t_+ + t_- = 1$, the conservation equation is

$$\epsilon \frac{\partial c}{\partial t} = \nabla \cdot (\epsilon D_{amb} \nabla c) + \nabla \cdot \left(\frac{(1 - t_+) \mathbf{i}}{e} \right). \tag{52}$$

Substituting Equation (51) into Equation (52), the familiar Porous Electrode Theory equation,

$$\epsilon \frac{\partial c}{\partial t} + a_p j_{in} = \nabla \cdot (\epsilon D_{amb} \nabla c) - \nabla \cdot \left(\frac{t_+ \mathbf{i}}{e} \right), \tag{53}$$

is derived. Since the potential was eliminated in the ambipolar derivation, and the potential gradient is dependent on the current density via Equation (50), Equations (50) and (51) can be used to formulate an expression for the local electrolyte potential,

$$a_p j_{in} = \nabla\cdot\left[\left(D_+ - D_-\right)\epsilon\nabla c + \frac{e^2}{k_B T}\left(z_+ D_+ + z_- D_-\right)\epsilon c\nabla\phi\right]. \tag{54}$$

Finally, an expression for j_{in} is required to complete the set of equations. This can be modeled via the Butler-Volmer Equation.

For phase transforming materials, the activity of the particles and energy of the transition state can have a dramatic effect on the reaction rate. To account for this, a modified form of the Butler-Volmer Equation, which accounts for the energy of the transition state, will be derived.

2. Faradaic Reaction Kinetics

The reader is referred to Bazant [10, 11] for detailed, pedagogical derivations of Faradaic reaction rates in concentrated solutions and solids, generalizing both the phenomenological Butler-Volmer equation [24] and the microscopic Marcus theory of charge transfer [8, 82, 89]. Here we summarize the basic derivation and focus applications to the case of lithium intercalation in a solid solution.

In the most general Faradaic reaction, there are n electrons transferred from the electrode to the oxidized state O to produce the reduced state R:

$$\mathrm{O} + ne^- \rightleftharpoons \mathrm{R}.$$

Typically, one electron transfer is favored [8, 24, 82], but for now let us keep the derivation as general as possible. The reaction goes through a transition state, which involves solvent reorganization and charge transfer. The net reaction rate, R_{net}, is the sum of the forward and reverse reaction rates,

$$R_{net} = k\left[\exp\left(-\frac{\mu_\ddagger^{ex} - \mu_1}{k_B T}\right) - \exp\left(-\frac{\mu_\ddagger^{ex} - \mu_2}{k_B T}\right)\right]. \tag{55}$$

Only the excess of the chemical potential of the transition state is important, as reactions are considered to be rare events, and concentrations of the transition state should not have a large effect on the energy landscape. This allows the transition state concentration to be factored into the rate constant.

It is first necessary to postulate forms of the chemical potentials in the generic Faradaic reaction above. Here it is assumed that both the oxidant and reductant are charged species, and that the electron is at a potential ϕ_M, which is the potential of the conducting phase (e.g. carbon black). The chemical potentials of the oxidant and reductant are

$$\mu_O = k_B T\ln a_O + eq_O\phi - ne\phi_M + E_O, \text{ and} \tag{56}$$
$$\mu_R = k_B T\ln a_R + eq_R\phi + E_R, \tag{57}$$

where E_O and E_R are the reference energies of the oxidant and reductant, respectively. The excess chemical potential of the transition state is assumed to consist of some activity coefficient and some linear combination of the potentials of the oxidant and reductant,

$$\mu_\ddagger^{ex} = k_B T\ln\gamma_\ddagger + \alpha eq_R\phi + (1-\alpha)e\left(q_O\phi - n\phi_M\right) + E_\ddagger, \tag{58}$$

where α, also known as the transfer coefficient, denotes the symmetry of the transition state. This value is typically between 0 and 1. The postulated forms of the chemical potential can be simplified for the lithium-ion battery system. The charge of the reductant, q_R, is 0. Also, the potential difference $\phi_M - \phi$ is defined as $\Delta\phi$. Finally, the chemical potential is scaled by the thermal energy, $k_B T$. The postulated forms of the chemical potential are

$$\tilde{\mu}_O = \ln a_O - \Delta\tilde{\phi} + \tilde{E}_O, \tag{59}$$
$$\tilde{\mu}_R = \ln a_R + \tilde{E}_R, \text{ and} \tag{60}$$
$$\tilde{\mu}_\ddagger^{ex} = \ln\gamma_\ddagger - (1-\alpha)\Delta\tilde{\phi} + \tilde{E}_\ddagger, \tag{61}$$

where $\tilde{\phi}$ is the dimensionless potential, $\frac{e\phi}{k_B T}$. It is important to note that at equilibrium (i.e. $\tilde{\mu}_O = \tilde{\mu}_R$), the Nernst Equation,

$$\Delta\tilde{\phi}_{eq} = \left(\tilde{E}_O - \tilde{E}_R\right) - \ln\frac{a_R}{a_O}, \tag{62}$$

is obtained. Equations (59), (60), and (61) can be substituted directly into Equation (55) to obtain the reaction rate,

$$R = \frac{k_o}{\gamma_\ddagger}\left[a_O\exp\left(\tilde{E}_O - \tilde{E}_\ddagger\right)\exp\left(-\alpha\Delta\tilde{\phi}\right) - a_R\exp\left(\tilde{E}_R - \tilde{E}_\ddagger\right)\exp\left(\right.\right. \tag{63}$$

Next, the definition of overpotential is substituted into Equation (63). The overpotential is defined as

$$\tilde{\eta} \equiv \Delta\tilde{\phi} - \Delta\tilde{\phi}_{eq}. \tag{64}$$

After simplifying, we arrive at the classical Butler-Volmer Equation,

$$ej_{in} = i_o\left[\exp\left(-\alpha\tilde{\eta}\right) - \exp\left(\left(1-\alpha\right)\tilde{\eta}\right)\right], \tag{65}$$

where i_o, the exchange current density, is defined as

$$i_o = \frac{e\left(k_c^o a_O\right)^{1-\alpha}\left(k_a^o a_R\right)^{\alpha}}{\gamma_\ddagger}. \tag{66}$$

The only difference is that we have defined the overpotential and exchange current in terms of the activities of the oxidized, reduced and transition states, each of which can be expressed variationally in terms of the total free

energy functional o the system (below). In Equation (66), the constants k_c^o and k_a^o are

$$k_c^o = \exp\left(\tilde{E}_O - \tilde{E}_\ddagger\right), \text{ and} \tag{67}$$

$$k_a^o = \exp\left(\tilde{E}_R - \tilde{E}_\ddagger\right). \tag{68}$$

(Note: k_o, the rate constant, can be factored out) Using the Butler-Volmer Equation, the value of j_{in} (the flux into the particles due to Faradaic reactions) can be modeled. The overpotential is calculated via the definition given in Equation (64), and the equilibrium potential is given by the Nernst Equation, where the activity of surface of the active material is used.

3. Potential Drop in the Conducting Solid Phase

The reaction rate at the surface of the particles is dependent on the potential of the electron as well as the potential of lithium in the electrolyte. This is expressed as $\Delta\phi$, which contributes to the overpotential in Equation (64). The potential difference is the difference between the electron and lithium-ion potential,

$$\Delta\phi = \phi_M - \phi,$$

where ϕ_M is the potential of the conducting (e.g. carbon black) phase and ϕ is the potential of the electrolyte. The potential of the electrolyte is determined by the charge conservation equation in Equation (51). To determine the potential drop in the conducting phase, we use current conservation which occurs throughout the entire electrode, given by

$$\mathbf{i} + \mathbf{i}_M = I/A_{sep}, \tag{69}$$

where $\mathbf{i}_M$ is the current density in the carbon black phase. For constant current discharge, the relation between the local reaction rate and the divergence of the current density in the conducting phase is

$$ea_p j_{in} = \nabla \cdot \mathbf{i}_M. \tag{70}$$

The current density in the conducting phase can be expressed using Ohm's Law. For a given conductivity of the conducting phase, the current density is

$$\mathbf{i}_M = -\sigma_m \nabla\phi. \tag{71}$$

The conductivity of the conducting phase can be modeled or fit to experiment based on porosity, the loading percent of the carbon black, and/or the lithium concentration in the solid,

$$\sigma_m = \sigma_m\left(\tilde{c}_s, L_p, \epsilon\right).$$

As lithium concentration increases in the particles, there are more electrons available for conduction. These are a few of the cell properties that can have a large impact on the conductivity of the solid matrix in the porous electrode.

4. Diffusion in the Solid

Proper handling of diffusion in the solid particles requires the use of concentrated solution theory. Diffusion inside solids is often non-linear, and diffusivities vary with local concentration due to finite volume and other interactions inside the solid. The first section on concetrated solution theory layed the groundwork for proper modeling of diffusion inside the solid. Here, we begin with the flux defined in Equation (36),

$$\mathbf{N}_i = -M_i c_i \nabla\mu_i,$$

where $\mathbf{N}_i$ is the flux of species i, M_i is the mobility, c_i is the concetration, and μ_i is the chemical potential. With no sink or source terms inside the particles, the mass conservation equation from Equation (37) is

$$\frac{\partial c_i}{\partial t} = -\nabla \cdot \mathbf{N}_i. \tag{72}$$

There are many different models which can be used for the chemical potential. A typical model used for the free energy is the regular solution model, which incorporates entropic and enthalpic effects. The regular solution model free energy is

$$g = k_B T\left[\tilde{c}_s \ln \tilde{c}_s + (1-\tilde{c}_s)\ln(1-\tilde{c}_s)\right] + \Omega \tilde{c}_s\left(1-\tilde{c}_s\right), \tag{73}$$

where $\tilde{c}_s$ is the dimensionless solid concentration ($\tilde{c}_s = c_s/c_{s,max}$). Figure 11 demonstrates the effect of the regular solution parameter (i.e. the pairwise interaction) on the free energy of the system. The model is capable of capturing the physics of homogeneous and phase separating systems.

Homogeneous particles demonstrate solid solution behavior, as all filling fractions are accessible. This behavior is typically indicated by a monotonically decreasing open circuit voltage curve. In terms of the regular solution model, a material that demonstrates solid solution behavior has a regular solution parameter of less than $2k_BT$, that is $\Omega < 2k_BT$. This is related to the free energy curve. When $\Omega \leq 2k_BT$, there is a single minimum in the free energy curve over the range of concentrations. However, for $\Omega > 2k_BT$, there are two minima, resulting in phase separation and a common tangent, which corresponds to changing fractions of each phase.

The common tangent construction arises from the fact that phases in equilibrium have the same chemical potential (i.e. slope). The chemical potential of the regular solution model is

$$\mu = \frac{\partial g_i}{\partial c_i} = k_B T \ln\left(\frac{\tilde{c}_s}{1-\tilde{c}_s}\right) + \Omega\left(1-2\tilde{c}_s\right). \tag{74}$$

To obtain an analogous equation to Fick's First Law, Equation (36) can be expressed as

$$\mathbf{N}_i = -D_o\left(1-\tilde{c}_s\right)\left(1+\frac{\partial \ln \gamma_i}{\partial \ln c_i}\right)\nabla c_i = -D_{chem}\nabla c_i, \tag{75}$$

where D_o is the diffusivity of species i in the infinitely dilute limit and D_{chem} is the chemical diffusivity in a concentrated solution. It is important to note that D_o can still be a function of concentration. The regular solution model in Equation (74) can be substituted into Equation (75) using the definition of the chemical potential, $\mu = k_B T \ln(c\gamma)$, to obtain an chemical diffusivity,

$$D_{chem} = D_o \left(1 - 2\tilde{\Omega}\tilde{c}_s + 2\tilde{\Omega}\tilde{c}_s^2\right), \tag{76}$$

where $\tilde{\Omega} = \Omega / k_B T$, the dimensionless interaction energy. When the interaction parameter, Ω, is zero, the dilute limit diffusivity (Fick's Law) is recovered. The mass conservation equation using the effective diffusivity is

$$\frac{\partial c_s}{\partial t} = \nabla \cdot \left(D_{chem} \nabla c_s\right). \tag{77}$$

Phase separating materials (e.g. $LiFePO_4$) require the use of the Cahn-Hilliard free energy functional.[32] This is because phase separation causes "uphill diffusion". To account for this, a gradient penalty term is included. This term balances the interfacial energy of a phase transformation with the bulk free energy. The Cahn-Hilliard free energy functional is

$$G[c(x)] = N_V \int_V \left[\overline{g}(c) + \frac{1}{2}\kappa \left(\nabla c\right)^2\right] dV, \tag{78}$$

where $\overline{g}\left(c\right)$ is the homogeneous free energy, and κ is the gradient energy, with units of energy times length squared. Note that the gradient energy is actually a symmetric tensor. Determining the chemical potential requires a variational derivative and use of the Euler-Lagrange Equation. The chemical potential is

$$\mu = \frac{\delta G}{\delta c} = \overline{\mu}\left(c\right) - \nabla \cdot \left(\kappa \nabla c\right), \tag{79}$$

where $\overline{\mu}$ is the homogeneous chemical potential. A typical double well free energy function (e.g. regular solution with $\Omega > 2k_BT$) can be used to model the homogeneous chemical potential. Determining the diffusion equation requires use of Equation (36). Using the Cahn-Hilliard form of the free energy, the flux becomes

$$\mathbf{N}_i = -Mc\left[\nabla \overline{\mu}\left(c\right) - \kappa \nabla^3 c\right], \tag{80}$$

assuming κ is constant. Inserting our flux equation into Equation (72), the conservation equation based on the Cahn-Hilliard form of the free energy is

$$\frac{\partial c}{\partial t} = \nabla \cdot \left(Mc \nabla \overline{\mu}\right) - \nabla \cdot \left(Mc\kappa \nabla^3 c\right). \tag{81}$$

This conservation equation contains a fourth derivative of concentration, requiring the use of another boundary condition. The condition used is that the gradient penalty at the surface of the solid is zero. Two examples of diffusion in the solid based on concentrated solution theory have been given. The Cahn-Hilliard form is more general and can be used for any material, while the regular solution is explicity for use in solid solution materials.

The choice of the gradient and divergence operators is dependent upon the selected geometry of the particles. To complete the modeling of the particles, we impose two flux conditions. One at the surface and the other at the interior of the particle. For example, consider a spherical particle with a radius of 1. The boundary conditions are

$$\left.\frac{\partial c}{\partial r}\right|_{r=0} = 0, \text{ and} \tag{82}$$

$$-D_s \left.\frac{\partial c}{\partial r}\right|_{r=1} = j_{in}, \tag{83}$$

where D_s is the solid diffusivity (can be a function of concentration). These equations demonstrate the symmetry condition at the interior of the particle, and the relation to the reaction rate at the surface of the particle, which comes from the modified Butler-Volmer Equation.

5. Modeling the Equilibrium Potential

To complete the model, a form of the open circuit potential (OCP) is required. While traditional battery models fit the OCP to discharge data, the OCP is actually a function of the thermodynamics of the material. The OCP can be modeled using the Nernst Equation given in Equation (62),

$$\Delta\phi_{eq} = V^o - \frac{k_B T}{ne} \ln\left(\frac{a_R}{a_O}\right),$$

where V^o is the standard potential. Typically, we take lithium metal as the reference potential for the anode and cathode materials. For the cathode material, this allows us to treat the activity of the oxidant as a constant. Let's again consider the regular solution model. Using the definition for chemical potential, $\mu \equiv k_B T \ln a$, we substitute in our regular solution chemical potential to get

$$\Delta\phi_{eq} = V^o - \frac{k_B T}{e} \ln\left(\frac{\tilde{c}_s}{1-\tilde{c}_s}\right) - \frac{\Omega}{e}\left(1 - \tilde{c}_s\right). \tag{84}$$

Figure 12 shows open circuit potential curves for different regular solution parameter values. For $\Omega > 2k_BT$, the system is phase separating. This corresponds to a non-monotonic voltage diagram.

Since the reaction occurs at the surface, and the concentration inside the solid is not necessarily uniform, then surface concentration determines the local OCP. This in turn affects the overpotential and the reaction rate. Larger overpotentials are required when the solid has a slow diffusivity. As lithium builds up at the surface of the particle, a higher overpotential is required to drive the intercalation reaction.

B. Non-Dimensionalization and Scaling

In this section, the equations are non-dimensionalized for the full three dimensional case. The electrode is assumed to have a constant cross sectional area, which is typical in rolled electrodes where the area of the separator is much larger than the electrode thickness. The total current is the sum of the fluxes into the particles in the electrode. This is represented by the integral equation

$$I = \int_{A_s} F j_{in} dA_s = \int_{V_s} F a_p j_{in} dV_s, \tag{85}$$

where a_p is the area per volume of the particles. The solid volume, V_s, can be expressed as $(1-\epsilon) L_p V$, where ϵ is the porosity, L_p is the volume fraction of active material, and V is the volume of the cell. Scaling the time by the diffusive time, $t_d = L^2/D_{amb}$, and the charge by the capacity of the entire electrode, the dimensionless current is

$$\tilde{I} = \frac{I t_d}{F(1-\epsilon) L_p V c_{s,max}} = \int_{\tilde{V}} \tilde{j_{in}} d\tilde{V}, \tag{86}$$

where the dimensionless reaction flux, $\tilde{j}_{in}$, is defined as

$$\tilde{j}_{in} = \frac{a_p j_{in} t_d}{c_{s,max}}. \tag{87}$$

The non-dimensional current density in the electrolyte is

$$\tilde{\mathbf{i}} = -\left(\tilde{D}_+ - \tilde{D}_-\right) \tilde{\nabla} \tilde{c} - \left(z_+ \tilde{D}_+ + z_- \tilde{D}_-\right) \tilde{c} \tilde{\nabla} \tilde{\phi}, \tag{88}$$

where the dimensionless current density $\tilde{\mathbf{i}}$ is defined as

$$\tilde{\mathbf{i}} = \frac{t_d \mathbf{i}}{L F c_o}. \tag{89}$$

Similarly, the non-dimensional charge conservation equation becomes

$$\beta \tilde{j_{in}} = -\tilde{\nabla} \cdot \tilde{\mathbf{i}}, \tag{90}$$

where $\beta = V_s c_{s,max}/V_e c_o$ is the ratio of lithium capacity in the solid to initial lithium in the electrolyte. This parameter is important, as it determines the type of cell. For $\beta \ll 1$, the system has essentially no storage capability, and the equations are typically used to model capacitors. At $\beta \approx 1$, the system has comparable storage in the electrolyte and solid. This is typically seen in pseudocapacitors. The equations for systems like these typically include a term for double layer charge storage as well. For $\beta \gg 1$, there is a large storage capacity in the solid, which is typically found in batteries.

Next, a mass balance on the electrolyte and solid are performed. Equation (53) is non-dimensionalized for some control volume inside the electrode. In this control volume, the electrolyte and solid volumes are represented by V_e and V_s, respectively. It is assumed that the electrode has the same properties thoughout (e.g. porosity, loading percent, area per volume, etc.). The dimensionless mass balance is

$$V_e \frac{\partial c}{\partial t} + V_s a_p j_{in} = V_e \nabla \cdot (D_{amb} \nabla c) - V_e \nabla \cdot \left(\frac{t_+ \mathbf{i}}{F}\right), \tag{91}$$

where the time is scaled by the diffusive time scale, t_d, the gradients are scaled by the electrode length, L, the diffusivity is scaled by the dilute limit ambipolar diffusivity, $D_{amb,o}$, the electrolyte concentration is scaled by the initial electrolyte concentration, c_o, and the current density, j_{in}, is scaled as in Equation (87). Simplifying yields

$$\frac{\partial \tilde{c}}{\partial \tilde{t}} + \beta \tilde{j_{in}} = \tilde{\nabla} \cdot \left(\tilde{D}_{amb} \tilde{\nabla} \tilde{c}\right) - \tilde{\nabla} \cdot \left(t_+ \tilde{\mathbf{i}}\right). \tag{92}$$

Next, we need to find the dimensionless boundary conditions for the system. This can be done via integrating the equations over the volume of the cell (in this case the separator and cathode, but this can easily be extended to include the anode). Integrating Equation (92) over the volume yields

$$\int_{\tilde{V}} \left[\frac{\partial \tilde{c}}{\partial \tilde{t}} + \beta \tilde{j_{in}} = \tilde{\nabla} \cdot \left(\tilde{D}_{amb} \tilde{\nabla} \tilde{c}\right) - \tilde{\nabla} \cdot \left(t_+ \tilde{\mathbf{i}}\right)\right] d\tilde{V}. \tag{93}$$

First, we deal with the left most term. Given the electroneutrality constraint, this term becomes zero because the amount of anions in the system remains constant. Integrating the second term, for constant β, reduces to $\beta \tilde{I}$. The two terms on the right hand side of the equation facilitate the use of the Fundamental Theorem of Calculus. Simplifying, we obtain

$$\beta \tilde{I} = \left(\tilde{D}_{amb} \tilde{\nabla} \tilde{c} - t_+ \tilde{\mathbf{i}}\right)\Big|_0^1. \tag{94}$$

Given the no flux conditions in $\tilde{y}$ and $\tilde{z}$, and the no flux condition at $\tilde{x} = 1$, the flux into the separator is

$$-\tilde{D}_{amb} \tilde{\nabla} \tilde{c}\Big|_{\tilde{x} = -\tilde{x}_s} = (1 - t_+) \beta \tilde{I}. \tag{95}$$

This set of dimensionless equations and boundary conditions are used in the simulations presented in the results section.

VII. MODEL RESULTS

To characterize the properties of the model, we will demonstrate some results from the non-dimensional model. Results for monotonic (i.e. homogeneous) and non-monotonic (i.e. phase separating) open circuit potential profiles for particles demonstrating solid solution behavior will be given for constant current discharge.

The electrolyte concentration, electrolyte potential, and solid concentration are all coupled via the mass and

charge conservation equations listed above. The system of equations was solved using MATLAB and its *ode15s* differential algebraic equation (DAE) solver. This code utilizes the backwards differentiation formula (BDF) for time stepping and a dogleg trust-region method for its implicit solution. The spatial equations were discretized using a finite volume method. Constant current discharge involves an integral constraint on the system. This integral constraint makes the system ideal for formulating the system of equations as a DAE. We hope to write a future paper detailing how to formulate the porous electrode theory equations for use as a DAE.

These results will try and focus on the important aspects of the model, which include electrolyte diffusion limited discharge and solid diffusion limited discharge. These two limitations represent the most common situations in a cell. Another common limitation is electron conductivity in the solid matrix. This limitation is often suppressed via proper cell design and increasing the amount of conductive additive used. Furthermore, some active materials naturally conduct electrons, alleviating this effect.

The electrolyte diffusion limitation can also be alleviated with proper cell design (i.e. thinner electrode), but this comes at the cost of capacity of the cell. To demonstrate the effect of electrolyte diffusivity limitations and solid diffusivity limitations, different discharge rates were selected and different solid diffusivities were modeled. First, we consider the case of homogeneous particles. Then we demonstrate phase separating particles using the Cahn-Hilliard free energy functional with and without approximated stress effects. Finally, we demonstrate the pseudocapacitor model for phase separating particles, which neglects solid diffusion.

A. Simulation Values

The ambipolar diffusivity (given by Equation (47)) is taken from literature values for the diffusivity of Li^+ and PF_6^- in an EC/EMC non-aqueous electrolyte. Using literature values for the diffusivities, a value of 1.9×10^{-10} m^2s^{-1} was calculated for $D_{amb,o}$. [38, 120] Suitable cell size parameters were used, including a cross sectional area of 1 cm^2, separator thickness of 25μm, and an electrode length of 50μm. A porosity value of 0.4 was used, which is a little larger than typical cell values. While cell dimensions are typically fixed, the ambipolar diffusivity and porosity values are flexible, and can be varied (within reason) to fit experimental data.

Using these cell dimensions and ambipolar diffusivity, the diffusive time scale for the system is 13.125 seconds. This value is important, as it affects the non-dimensional total current (which is scaled by the electrode capacity and the diffusive time), the non-dimensional current density, and the non-dimensional exchange current density (i.e. rate constant). Using this value of the ambipolar diffusivity, a dimensionless current of $\tilde{I} = 0.00364$ corresponds to approximately a 1C disharge. The solid diffusivity is incorporated in a dimensionless parameter,

$$\delta_d = \frac{L_s^2 D_{amb}}{L^2 D_s} \tag{96}$$

which is the ratio of the diffusion time in the solid (L_s^2/D_s) to the diffusion time in the electrolyte (L^2/D_{amb}). This parameter, which is typically typically larger than one, can vary by orders of magnitude for different materials. Typically, solid diffusivities are unknown, and this parameter needs to be fit to data.

The rate constant, which directly affects the exchange current density, is another value that is unknown in the system. The dimensionless value of the exchange current density is scaled to the diffusive time. It also depends on the average particle size, as this gives the surface area to volume ratio. For 50 nm particles, using the ambipolar diffusivity above, a dimensionless exchange current density of one corresponds to approximately 1.38 A/m^2. This is a relatively high exchange current density. For the simulations below, a dimensionless exchange current density of 0.01 is used.

B. Homogeneous Particles

Homogeneous particles can access all filling fractions as they are discharged. Figures 15, 17, and 18 demonstrate the effect of various discharge rates and solid diffusivities on the voltage profile. Each figure contains three different voltage plots. The red dots on the voltage curves indicate the filling fraction of the solid concentration contours below. The contour plots are arranged in the same order as the red dots, going from left to right, top to bottom. Figure 13 gives the axes for the simulations. Each particle is modeled in 1D, with the intercalation reaction at the top and diffusion into the bulk of the particle. The x_s axis is the depth into the particle.

The contour plots give the solid concentration profile of each volume of particles along the length of the electrode. The y-axis is the depth in the solid particle, with the top ($\tilde{y} = 1$) denoting the interface between the particle and the electrolyte. The x-axis denotes the depth into the electrode, with the left side represeting the separator-electrode interface and the right side representing the current collector. It is important to note that in order for lithium to travel horizontally, it must first diffuse through the solid, undergo a Faradaic reaction to leave the solid, diffuse through the electrolyte, then intercalate into another particle and diffuse. Therefore sharp concentration gradients in the x-direction are stable, especially for the case of non-monotonic voltage profiles, as is seen in phase separating materials.

Figure 15 demonstrates the effect of various discharge rates on the voltage. At $\tilde{I} = 0.001$ (C/3), the discharge is slow and the solid in the electrode fills homogeneously throughout. As the discharge rate is increased, increased overpotential follows. Furthermore, gradients in solid

concentration down the length of the electrode begin to emerge. Concentration gradients within the solid are not present because of the high solid diffusivity ($\delta_d = 1$, indicating the solid and electrolyte diffusive time scales are the same).

As the current is increased, gradients in solid concentration across the electrode begin to become prevalent. At the same time, transport limitations in the electrolyte lead to a capacity limitation, as the electrolyte is incapable of delivering lithium quickly enough deeper into the electrode. Figure 16 demonstrates the electrolyte depletion leading to the concentration polarization in the 15C discharge curve. While the voltages appears to stop, these are actually points where it drops off sharply. Tighter tolerances, which can significantly increase the computation time, are needed to get the voltage down to zero.

It is important to note that δ_d is not the ratio of diffusivities, but the ratio of diffusive times. Therefore, as particle size increases, the diffusive time scales as the square of the particle size. Solid diffusivities are typically much slower than in the electrolyte. To demonstrate the effect of increased current with slower solid diffusion, Figure 17 demonstrates the same discharge rates as the previous figure, except the solid diffusive time scale has been increased to 50 times the electrolyte diffusive time scale.

For decreased solid diffusivity, concentration gradients in the depth direction of the particles are more prevalent. At low current (i.e. slow discharge), the gradients in the electrode and particles are minimal. As the current is increased, gradients in the particles begin to emerge. At the fastest discharge rate, these solid concentration gradients become very large. Finite volume effects at the surface of the particles increase the overpotential substantially, producing a sharp voltage dropoff and low utilization. This effect is caused by the slow solid diffusion only. Despite plenty of lithium being available in the electrolyte, high surface concentrations block available sites for intercalation.

To show the effect of solid diffusion alone, Figure 18 demonstrates the effect of decreasing solid diffusivity at a constant discharge rate. When the diffusive time scales of the solid and electrolyte are comparable, each particle fills homogeneously. There are small variations along the length of the electrode, but these do not affect the utilization, as almost 100% of the electrode is utilized.

As the solid diffusivity is decreased, and the diffusive time scale approaches 50 times the electroloyte diffusive time scale, we see over a 10% drop is capacity. Concentration gradients in the solid particles begin to emerge. As the solid diffusivity is further decreased, and the solid diffusive time scale approaches 100 times the electrolyte diffusive time scale, the solid concentration gradients become quite large, leading to a 30% drop in capacity. While these changes in δ_d seem significant, they represent approximately a two order of magnitude change in diffusivity, and a one order of magnitude change in particle size.

C. Phase Separating Particles

For the case of phase separating materials, the equilibrium homogeneous voltage curve is non-monotonic. This is demonstrated in Figure 12, for regular solution parameters greater than $2k_BT$. For these materials, the free energy curve has two local minima. When the second derivative of the free energy with respect to filling fraction changes sign (positive to negative), the system is unstable for infinitessimal perturbations, resulting in phase separation. A tie line represents the free energy of the system, and the proportion of the two phases changes as the system fills.

Modeling phase separating materials requires the use of the Cahn-Hilliard free energy functional as given in Equation (78), and the Cahn-Hilliard diffusional chemical potential, given in Equation (79). When we insert the chemical potential into the modified Butler-Volmer Equation, we obtain a forced Allen-Cahn type equation. Here, we present the first solution of multiple phase separating particles in a porous electrode.

For phase separating particles, values of $\Omega = 4k_BT$ and $\tilde{\kappa} = 0.001$ were used along with a regular solution model to model the homogeneous chemical potential, $\overline{\mu}$. The same exchange current as above was used. The figures are similar to those of the homogeneous plots, but instead of the depth direction, we now plot along the surface. Figure 14 depicts the axes plotted. This assumes that the diffusion into the particle is fast, and that the process is essentially surface reaction limited. This is a reasonable approximation for $LiFePO_4$. [5] Figure 19 demonstrates slow discharge (approx. C/30).

Initially, the discrete filling of the electrode suppresses phase separation inside the particles. Towards of the end of the discharge, decreased electrolyte diffusion (from longer path length) allow for particles to phase separate. Another important feature of the simulation is the voltage spikes towards the end of the simulation. These voltage spikes, which are on the order of the thermal voltage, are an artifact of the discrete nature of the model. Towards the end of the simulation, only a few particles remain to fill, therefore the voltage is dominated by effectively the single particle response. Dreyer *et al.* demonstrated this previously for phase separating particles filling homogeneously. [49, 50] Recent work by Cogswell and Bazant demonstrate the importance of stress effects. [42]

Stress effects can be approximated by the inclusion of a term comparing local concentration to average particle concentration. This concept was first introduced by Cahn and Hilliard. [34–36] Including a volume averaged stress term, our chemical potential becomes

$$\mu = \overline{\mu} - \kappa\nabla^2 c_s + 2b\left(c_s - c_{s,avg}\right) \tag{97}$$

The inclusion of this additional term suppresses phase

separation by promoting homogeneous filling. When the difference between the local and average global particle concentration increases, the particle energy increases. This promotes homogeneous filling. Figure 20 demonstrates how this additional term suppresses phase separation.

Based on the work of Bai *et al.* [5], which demonstrated suppression of phase transformation in $LiFePO_4$ particles for discharge rates higher than the exchange current, this section will consider the case of phase transforming particles (namely $LiFePO_4$) that do not undergo phase transformation. That is, as the particles fill, each particle will fill homogeneously with a non-monotonic open circuit voltage profile.

Figure 21 demonstrates different discharge rates for phase separating particles with a regular solution parameter of $\Omega = 4.5k_BT$. The slowest discharge rate is a non-dimensional current of 0.00001. This corresponds to a real C-rate of approximately C/40. At this slow discharge rate, the particles fill discretely down the length of the electrode from the separator to the current collector. This discrete filling causes the voltage to oscillate back and forth between the voltage at the miscibility gap concentration (left part of the common tangent voltage) and the voltage of the spinodal point (voltage at the local minimum on the left side). While these spikes appear to be large, they are actually on the order of the thermal voltage or smaller. At typical voltage scales (2.0V-3.5V) these spikes are not seen, resulting in a flat voltage profile as seen in experimental data for $LiFePO_4$. This demonstrates that a phase separating material's flat voltage profile can be modeled without modeling phase transformation itself.

The voltage spikes are dependent on the value of the Damköhler number. At larger Damköhler numbers, the reaction time scale is faster than the diffusive time scale. The simulation begins with all particles at a filling fraction of 0.01. The electrode initially fills homogeneously to the voltage at the spinodal point. At this filling fraction, fewer particles are required to alleviate the discharge rate. To explain this, consider the equivalent circuit for a porous electrode in Figure 22.

Consider each of the "particles" in the equivalent circuit. Each particle (which could also be considered to be a cluster of particles with similar properties) has a charge transfer resistance, R_{ct}, and capacitance C. These values can be non-linear, and vary depending on the particle filling fraction and/or local potential. For each particle or cluster of particles, there is a charging time, τ, which scales as

$$\tau \sim R_{ct}C. \tag{98}$$

For a given discharge rate at constant current, particles in the electrode must alleviate a given amount of lithium per time in the electrode. The number of active particles scales as

$$n_{ap} \sim \tau \tilde{I}. \tag{99}$$

As the discharge rate is increased, the number of active particles increases until it spans the electrode, resulting in the electrode filling homogeneously. For fast kinetics or slow discharge rates, the number of active particles is small, which produces the discrete filling effect. For the non-monotonic OCP of homogeneous phase separating particles, the voltage plateau has three filling fractions that can exist in equilibrium: the left miscibility gap filling fraction, half filling fraction, and right miscibility gap filling fraction. As the particles fill, if the kinetics are sufficiently fast, then particles close to the active particle will empty to reach the equilibrium voltage (the plateau voltage). This increase in voltage for each particle as it deviates from the voltage at the spinodal concentration leads to an increase in cell voltage, producing the voltage spikes.

For slower kinetics, this effect is suppressed by two mechanisms. First, the charge transfer resistance is larger, leading to higher charging times and subsequently a larger number of active particles. Also, slower kinetics hinders the ability of particles to easily insert/remove lithium, which prevents the particles from emptying and increasing the voltage, leading to the spikes.

VIII. SUMMARY

In this paper, we have generalized porous electrode theory using principles of non-equilibrium thermodynamics. A unique feature is the use of Bazant's variational formulation of reaction kinetics [10, 11], which allows the use of phase field models to describe macroscopic phase transformations in porous electrodes for the first time. The thermodynamic consistency of all aspects of the model is crucial. Unlike existing battery simulation models, the open circuit voltage, reaction rate, and solid transport properties are not left free to be independently fitted to experimental data. Instead, these properties are all linked consistently to the electrochemical potentials of ions and electrons in the different components of the porous electrode. Moreover, emergent properties of a phase-separating porous electrode, such as its voltage plateau at low current, are not fitted to empirical functional forms, but rather follow from the microscopic physics of the material. This allows the model to capture stochastic, discrete phase transformation events, which are beyond the reach of traditional diffusion-based porous electrode theory.

In a companion paper [53], we will apply the model to predict the electrochemical behavior of composite, porous graphite anodes [62] and LFP cathodes [50], each of which have multiple stable phases. Complex nonlinear phenomena, such as narrow reaction fronts, mosaic instabilities, zero current voltage gap, and voltage fluctuations, naturally follow from the simple physics contained in the model. The model is able to fit experimental data for phase transformations in porous electrodes under very different conditions, limited either by electrolyte diffu-

sion [62] or by reaction kinetics [50].

This work was supported by the National Science Foundation under Contracts DMS-0842504 and DMS-0948071 (H. Warchall) and by a seed grant from the MIT Energy Initiative.

[1]
[2] S.M. Allen and J.W. Cahn. Microscopic theory for antiphase boundary motion and its application to antiphase domain coarsening. *Acta Metallurgica*, 27:10851095, 1979.
[3] H. Assadi. Phase-field modelling of electro-deoxidation in molten salt. *Modelling and Simulation in Materials Science and Engineering*, 14:963974, 2006.
[4] S. Atlung, K. West, and T. Jacobsen. Dynamic aspects of solid solution cathodes for electrochemical power sources. *Journal of the Electrochemical Society*, 126(8), 1979.
[5] Peng Bai, Daniel Cogswell, and Martin Z. Bazant. Suppression of phase separation in $LiFePO_4$ nanoparticles during battery discharge. *Nano Letters*, 11(11):4890–4896, 2011.
[6] N. Balke, S. Jesse, A. N. Morozovska, E. Eliseev, D. W. Chung, Y. Kim, L. Adamczyk, R. E. Garca, N. Dudney, and S. V. Kalinin. Nanoscale mapping of ion diffusion in a lithium-ion battery cathode. *Nature Nanotechnology*, 5, 2010.
[7] Robert W. Balluffi, Samuel M. Allen, and W. Craig Carter. *Kinetics of materials*. Wiley, 2005.
[8] A. J. Bard and L. R. Faulkner. *Electrochemical Methods*. J. Wiley & Sons, Inc., New York, NY, 2001.
[9] M. Z. Bazant. *Mathematical Modeling of Electrochemical Energy Systems*. Massachusetts Institute of Technology, 2009. lecture notes for subject 10.95.
[10] M. Z. Bazant. *10.626 Electrochemical Energy Systems*. Massachusetts Institute of Technology: MIT OpenCourseWare, http://ocw.mit.edu, License: Creative Commons BY-NC-SA, 2011.
[11] M. Z. Bazant. Theory of ion intercalation kinetics in batteries and fuel cells. *Accounts of Chemical Research*, to appear, 2012.
[12] M. Z. Bazant, K. T. Chu, and B. J. Bayly. Current-voltage relations for electrochemical thin films. *SIAM J. Appl. Math.*, 65:1463–1484, 2005.
[13] M. Z. Bazant, M. S. Kilic, B. D. Storey, and A. Ajdari. Nonlinear electrokinetics at large voltages. *New Journal of Physics*, 11:075016, 2009.
[14] M. Z. Bazant, M. S. Kilic, B.D. Storey, and A. Ajdari. Towards an understanding of nonlinear electrokinetics at large voltages in concentrated solutions. *Advances in Colloid and Interface Science*, 152:48–88, 2009.
[15] M. Z. Bazant, B. D. Storey, and A. A. Kornyshev. Double layer in ionic liquids: Overscreening versus crowding. *Phys. Rev. Lett.*, 106:046102, 2011.
[16] M. Z. Bazant, K. Thornton, and A. Ajdari. Diffuse charge dynamics in electrochemical systems. *Phys. Rev. E*, 70:021506, 2004.
[17] M. Biesheuvel, A. A. Franco, and M. Z. Bazant. Diffuse-charge effects in fuel-cell membranes. *Journal of the Electrochemical Society*, 156:B225–B233, 2009.
[18] P. M. Biesheuvel and J. Lyklema. Sedimentation–diffusion equilibrium of binary mixtures of charged colloids including volume effects. *J. Phys. Condens. Matter*, 17:6337, 2005.
[19] P. M. Biesheuvel and M. van Soestbergen. Counterion volume effects in mixed electrical double layers. *Journal of Colloid and Interface Science*, 316:490–499, 2007.
[20] P.M. Biesheuvel and M.Z. Bazant. Nonlinear dynamics of capacitive charging and desalination by porous electrodes. *Physical Review E*, 81, 2010.
[21] P.M. Biesheuvel, Y. Fu, and M.Z. Bazant. Diffuse charge and faradaic reactions in porous electrodes. *Physical Review E*, 83, 2011.
[22] P.M. Biesheuvel, Y. Fu, and M.Z. Bazant. Electrochemistry and capacitive charging of porous electrodes in asymmetric multicomponent electrolytes. *Russian Journal of Electrochemistry*, 2012.
[23] P.M. Biesheuvel, R. Zhao, S. Porada, and A. van der Wal. Theory of membrane capacitive deionization including the effect of the electrode pore space. *Journal of Colloid and Interface Science*, 360:239248, 2011.
[24] J. O.'M Bockris and A. K. N. Reddy. *Modern Electrochemistry*. Plenum, New York, 1970.
[25] W.J. Boettinger, S.R. Coriell, A.L. Greer, A. Karma, W. Kurz, M. Rappaz, and R. Trivedi. Solidification microstructures: Recent developments, future directions. *Acta Materialia*, 48:4370, 2000.
[26] W.J. Boettinger and J.A. Warren. The phase-field method: Simulation of alloy dendritic solidification during recalescence. *Metallurgical and Materials Transactions A*, 27:657669, 1996.
[27] W.J. Boettinger, J.A. Warren, C. Beckermann, and A. Karma. Phase-field simulation of solidification. *Annual Review of Materials Research*, 32:163194, 2002.
[28] A. Bonnefont, F. Argoul, and M.Z. Bazant. Analysis of diffuse-layer effects on time-dependent interfacial kinetics. *J. Electroanal. Chem.*, 500:52–61, 2001.
[29] Damian Burch. *Intercalation Dynamics in Lithium-Ion Batteries*. Ph.D. Thesis in Mathematics, Massachusetts Institute of Technology, 2009.
[30] Damian Burch and Martin Z. Bazant. Size-dependent spinodal and miscibility gaps for intercalation in nanoparticles. *Nano Letters*, 9(11):3795–3800, 2009.
[31] Damian Burch, Gogi Singh, Gerbrand Ceder, and Martin Z. Bazant. Phase-transformation wave dynamics $LiFePO_4$. *Solid State Phenomena*, 139:95–100, 2008.
[32] J. W. Cahn and J. W. Hilliard. Free energy of a nonuniform system: I. interfacial energy. *J. Chem Phys.*, 28:258–267, 1958.
[33] John Cahn. Free energy of a nonuniform system. ii. thermodynamic basis. *Journal of Chemical Physics*, 30(5):1121–1124, 1959.
[34] John Cahn. On spinodal decomposition. *Acta Metallurgica*, 9(9):795–801, 1961.
[35] John Cahn. Coherent fluctuations and nucleation in isotropic solids. *Acta Metallurgica*, 10, 1962.
[36] John Cahn. On spinodal decomposition in cubic crystals. *Acta Metallurgica*, 10, 1962.

[37] John Cahn and John Hilliard. Free energy of a nonuniform system. iii. nucleation in a two-component incompressible fluid. *Journal of Chemical Physics*, 31(3):688–699, 1959.

[38] C. Capiglia, Y. Saito, H. Kageyama an dP. Mustarelli, T. Iwamoto, T. Tabuchi, and H. Tukamoto. Li and f diffusion coefficients and thermal properties of nonaqueous electrolyte solutions for rechargeable lithium batteries. *Journal of Power Sources*, 81-82:859–862, 1999.

[39] G. Ceder, Y.-M. Chiang, D.R. Sadoway, M.K. Aydinol, Y.-I. Jang, and B. Huang. Identification of cathode materials for lithium batteries guided by first-principles calculations. *Nature*, 392:694–696, 1998.

[40] Guoying Chen, Xiangyun Song, and Thomas Richardson. Electron microscopy study of the $LiFePO_4$ to $FePO_4$ phase transition. *Electrochemical and Solid State Letters*, 9(6):A295–A298, 2006.

[41] L. Q. Chen. Phase-field models for microstructural evolution. *Annual Review of Materials Research*, 32:113–140, 2002.

[42] Daniel A. Cogswell and Martin Z. Bazant. Coherency strain and the kinetics of phase separation in $LiFePO_4$ nanoparticles. *ACS Nano*, 2012.

[43] S. Dargaville and T.W. Farrell. Predicting active material utilization in $LiFePO_4$ electrodes using a multiscale mathematical model. *Journal of the Electrochemical Society*, 157(7):A830–A840, 2010.

[44] R. de Levie. On porous electrodes in electrolyte solutions. *Electrochimica Acta*, 8:751–780, 1963.

[45] R. de Levie. On porous electrodes in electrolyte solutions - iv. *Electrochimica Acta*, 9:1231–1245, 1964.

[46] C. Delmas, M. Maccario, L. Croguennec, F. Le Cras, and F. Weill. Lithium deintercalation of $LiFePO_4$ nanoparticles via a domino-cascade model. *Nature Materials*, 7:665–671, 2008.

[47] Marc Doyle, Thomas F. Fuller, and John Newman. Modeling of galvanostatic charge and discharge of the lithium/polymer/insertion cell. *Journal of the Electrochemical Society*, 140(6):1526–1533, 1993.

[48] Marc Doyle, Antoni S. Gozdz, Caroline N. Schmuts, Jean-Marie Tarascon, and John Newman. Comparison of modeling predictions with experimental data from plastic lithium ion cells. *Journal of the Electrochemical Society*, 143(6), 1996.

[49] D. Dreyer, C. Guhlke, and R. Huth. The behavior of a many-particle electrode in a lithium-ion battery. *Physica D*, 240:1008–1019, 2011.

[50] Wolfgang Dreyer, Janko Jamnik, Clemens Guhlke, Robert Huth, Joze Moskon, and Miran Gaberscek. The thermodynamic origin of hysteresis in insertion batteries. *Nat. Mater.*, 9:448–453, 2010.

[51] M. Eikerling, A. A. Kornyshev, and E. Lust. Optimized structured of nanoporous carbonbased double-layer capacitors. *J. Electrochem. Soc.*, 152:E24, 2005.

[52] J. Euler and W. Nonnenmacher. Current distribution in porous electrodes. *Electrochimica Acta*, 2:268–286, 1960.

[53] Todd R. Ferguson and Martin Z. Bazant. Theory of macroscopic phase transformations in porous electrodes. 2012. in preparation.

[54] Thomas Fuller, Marc Doyle, and John Newman. Simulation and optimization of the dual lithium ion insertion cell. *Journal of the Electrochemical Society*, 141(1):1–10, 1994.

[55] R. Edwin Garcia and Yet-Ming Chiang. Spatially resolved modeling of microstructurally complex battery architectures. *Journal of the Electrochemical Society*, 154(9):A856–A864, 2007.

[56] R. Edwin Garcia, Yet-Ming Chiang, W. Craig Carter, Pimpa Limthongkul, and Catherine M. Bishop. Microstructural modeling and design of rechargeable lithium-ion batteries. *Journal of the Electrochemical Society*, 152(1):A255–A263, 2005.

[57] S. R. De Groot and P. Mazur. *Non-equilibrium Thermodynamics*. Interscience Publishers, Inc., New York, NY, 1962.

[58] I.G. Gurevich and V.S. Bagotzky. Steady-state operation of a porous electrode polarized from one side with diffusion supply of liquid reactants from both sides. *Electrochimica Acta*, 12:593–614, 1967.

[59] J.E. Guyer, W.J. Boettinger, J.A. Warren, and G.B. McFadden. *Physical Review E*, 69:021603, 2004.

[60] J.E. Guyer, W.J. Boettinger, J.A. Warren, and G.B. McFadden. *Physical Review E*, 69:021604, 2004.

[61] B.C. Han, A. Van der Ven, D. Morgan, and G. Ceder. Electrochemical modeling of intercalation processes with phase field models. *Electrochimica Acta*, 49:4691–4699, 2004.

[62] Stephen J. Harris, Adam Timmons, Daniel R. Baker, and Charles Monroe. Direct in situ measurements of li transport in li-ion battery negative electrodes. *Chemical Physics Letters*, 485:265274, 2010.

[63] Kuei-Feng Hsu, Sun-Yuan Tsay, and Bing-Joe Hwang. Synthesis and characterization of nano-sized $LiFePO_4$ cathode materials prepared by a citric acid-based sol-gel route. *Journal of Materials Chemistry*, 14:2690–2695, 2004.

[64] H. Huang, S.C.Yin, and L.F. Nazar. Approaching theoretical capacity of $LiFePO_4$ at room temperature at high rates. *Electrochemical and Solid State Letters*, 4(10):A170–A172, 2001.

[65] R. A. Huggins. *Advanced Batteries: Materials Science Aspects*. Springer, 2009.

[66] E.A. Grens II. On the assumptions underlying theoretical models for flooded porous electrodes. *Electrochimica Acta*, 15:1047–1057, 1970.

[67] E.A. Grens II and C.W. Tobias. The influence of electrode reaction kinetics on the polarization of flooded porous electrodes. *Electrochimica Acta*, 10:761–772, 1965.

[68] E. M. Itskovich, A. A. Kornyshev, and M. A. Vorotyntsev. Electric current across the metal-solid electrolyte interface. i. direct current, current-voltage characteristic. *phys. stat. sol. (a)*, 39:229–238, 1977.

[69] J. Jamnik and J. Maier. Generalised equivalent circuits for mass and charge transport : chemical capacitance and its implications. *Phys. Chem. Chem. Phys.*, 3:1668–1678, 2001.

[70] A. M. Johnson and John Newman. Desalting by means of porous carbon electrodes. *J. Electrochem. Soc.*, 118:510–517, 1971.

[71] Byoungwoo Kang and Gerbrand Ceder. Battery materials for ultrafast charging and discharging. *Nature*, 458:190–193, 2009.

[72] A. Karma. Phase-field model of eutectic growth. *Physical Review E*, 49:22452250, 1994.

[73] Dirk Kehrwald, Paul R. Shearing, Nigel P. Brandon,

Puneet K. Sinha, and Stephen J. Harris. Local tortuosity inhomogeneities in a lithium battery composite electrode. *Journal of the Electrochemical Society*, 158(12):A1393–A1399, 2011.

[74] M. S. Kilic, M. Z. Bazant, and A. Ajdari. Steric effects in the dynamics of electrolytes at large applied voltages: I double-layer charging. *Phys. Rev. E*, 75:021502, 2007.

[75] M. S. Kilic, M. Z. Bazant, and A. Ajdari. Steric effects on the dynamics of electrolytes at large applied voltages: II modified nernst-planck equations. *Phys. Rev. E*, 75:021503, 2007.

[76] A. A. Kornyshev and M. A. Vorotyntsev. Conductivity and space charge phenomena in solid electrolytes with one mobile charge carrier species, a review with original material. *Electrochimica Acta*, 26:303–323, 1981.

[77] O.S. Ksenzhek. Macrokinetics of processes on porous electrodes. *Electrochimica Acta*, 9:629–637, 1964.

[78] O.S. Ksenzhek and V.V. Stender. *Doklady Akademiia nauk SSSR*, 106:486, 1956.

[79] O.S. Ksenzhek and V.V. Stender. *Doklady Akademiia nauk SSSR*, 107:280, 1956.

[80] O.S. Ksenzhek and V.V. Stender. *Zhurnal prikladnoi khimii*, 32:110, 1959.

[81] Karthikeyan Kumaresan, Yuriy Mikhaylik, and Ralph E. White. A mathematical model for a lithiumsulfur cell. *Journal of The Electrochemical Society*, 155:A576–A582, 2008.

[82] A. M. Kuznetsov and J. Ulstrup. *Electron Transfer in Chemistry and Biology: An Introduction to the Theory*. Wiley, 1999.

[83] W. Lai and F. Ciucci. Thermodynamics and kinetics of phase transformation in intercalation battery electrodes phenomenological modeling. *Electrochim. Acta*, 56:531–542, 2010.

[84] W. Lai and S. M. Haile. Impedance spectroscopy as a tool for chemical and electrochemical analysis of mixed conductors: A case study of ceria. *J. Amer. Cer. Soc.*, 88:2979–2997, 2005.

[85] Wei Lai. Electrochemical modeling of single particle intercalation battery materials with different thermodynamics. *Journal of Power Sources*, 196:65346553, 2011.

[86] Wei Lai and Francesco Ciucci. Mathematical modeling of porous battery electrodes - revisit of newman's model. *Electrochimica Acta*, 56:4369–4377, 2011.

[87] Rahul Malik, Damian Burch, Martin Bazant, and Gerbrand Ceder. Particle size dependence of the ionic diffusivity. *Nano Letters*, 10:4123–4127, 2010.

[88] Rahul Malik, Fei Zhou, and Gerbrand Ceder. Kinetics of non-equilibrium lithium incorporation in $LiFePO_4$. *Nature Materials*, 10:587–590, 2011.

[89] R. A. Marcus. Electron transfer reactions in chemistry. theory and experiment. *Rev. Mod. Phys.*, 65:599–610, 1993.

[90] Graeme Walter Milton. *The Theory of Composites*. Cambridge University Press, 2002.

[91] D. Morgan, A. Van der Ven, and G. Ceder. Li conductivity in Li_xMPO_4 (m=mn,fe,co,ni) olivine materials. *Electrochemical and Solid State Letters*, 7(2):A30–A32, 2004.

[92] E. Bruce Nauman and D. Qiwei Heb. Nonlinear diffusion and phase separation. *Chemical Engineering Science*, 56:19992018, 2001.

[93] J. Newman. *Electrochemical Systems*. Prentice-Hall, Inc., Englewood Cliffs, NJ, second edition, 1991.

[94] John Newman and William Tiedemann. Porous-electrode theory with battery applications. *AIChE Journal*, 21(1):25–41, 1975.

[95] John Newman and Charles Tobias. Theoretical analysis of current distribution in porous electrodes. *Journal of The Electrochemical Society*, 109(12):1183–1191, 1962.

[96] L. H. Olesen, M. Z. Bazant, and H. Bruus. Strongly nonlinear dynamics of electrolytes in large ac voltages. *Phys. Rev. E*, 82:011501, 2010.

[97] Gosuke Oyama, Yuki Yamada, Ryu ichi Natsui, Shin ichi Nishimura, and Atsuo Yamada. Kinetics of nucleation and growth in two-phase electrochemical reaction of lixfepo4. *J. Phys. Chem. C*, 2012.

[98] A.K. Padhi, K.S. Nanjundaswamy, and J.B. Goodenough. Phospho-olivines as positive-electrode materials for rechargeable lithium batteries. *Journal of the Electrochemical Society*, 144(4):1188–1194, 1997.

[99] Mauro Pasquali, Alessandro DellEra, and Pier Paolo Prosini. Fitting of the voltageli+ insertion curve of lifepo4. *J Solid State Electrochem*, 13:18591865, 2009.

[100] R. Pollard and J. Newman. Transient behavior of porous electrodes with high exchange current densities. *Electrochimica Acta*, 25:315–321.

[101] S. Porada, L. Weinstein, R. Dash, A. van der Wal, M. Bryjak, Y. Gogotsi, and P.M. Biesheuvel. Water desalination using capacitive deionization with microporous carbon electrodes. *ACS Appl. Mater. Interfaces*, 4:1194?1199, 2012.

[102] Venkatasailanathan Ramadesigan, Paul W. C. Northrop, Sumitava De, Shriram Santhanagopalan, Richard D. Braatz, and Venkat R. Subramanian. Modeling and simulation of lithium-ion batteries from a systems engineering perspective. *Journal of The Electrochemical Society*, 159:R31–R45, 2012.

[103] S.K. Rangarajan. Theory of flooded porous electrodes. *Electroanalytical Chemistry and Interfacial Electrochemistry*, 22:89–104, 1969.

[104] N. Ravet, Y. Chouinard, J.F. Morgan, S. Besner, M. Gauthier, and M. Armand. Electroactivity of natural and synthetic triphylite. *Journal of Power Sources*, 97-98:503–507, 2001.

[105] Muhammad Sahimi. *Heterogeneous Materials I Linear Transport and Optical Properties*, volume 22 of *Interdisciplinary Applied Mathematics*. Springer, 2003.

[106] Y. Shibuta, Y. Okajima, and T. Suzuki. A phase-field simulation of bridge formation process in a nanometer-scale switch. *Scripta Materialia*, 55:10951098, 2006.

[107] G. K. Singh, M. Z. Bazant, and G. Ceder. Anisotropic surface reaction limited phase transformation dynamics in $lifepo_4$. arXiv:0707.1858v1 [cond-mat.mtrl-sci], 2007.

[108] Gogi Singh, Damian Burch, and Martin Z. Bazant. Intercalation dynamics in rechargeable battery materials: General theory and phase-transformation waves in $LiFePO_4$. *Electrochimica Acta*, 53:7599–7613, 2008.

[109] Madeleine Smith, R. Edwin Garcia, and Quinn C. Horn. The effect of microstucture on the galvanostatic discharge of graphite anode electrodes in $LiCoO_2$-based rocking-chair rechargeable batteries. *Journal of the Electrochemical Society*, 156(11):A896–A904, 2009.

[110] Venkat Srinivasan and John Newman. Discharge model for the lithium iron-phosphate electrode. *Journal of the Electrochemical Society*, 151(101):A1517–A1529, 2004.

[111] B. D. Storey, Lee R. Edwards, M. S. Kilic, and M. Z. Bazant. Steric effects on ac electro-osmosis in dilute

electrolytes. *Phys. Rev. E*, 77:036317, 2008.
[112] Ke Sun and Shen J. Dillon. A mechanism for the improved rate capability of cathodes by lithium phosphate surficial films. *Electrochemistry Communications*, 13:200–202, 2011.
[113] Ming Tang, James F. Belak, and Milo R. Dorr. Anisotropic phase boundary morphology in nanoscale olivine electrode particles. *The Journal of Physical Chemistry C*, 115:4922–4926.
[114] J.M. Tarascon and M. Armand. Issues and challenges facing rechargeable lithium batteries. *Nature*, 414:359–367, 2001.
[115] Ralf Theidmann, Ole Stenzel, Aaron Spettl, Paul R. Shearing, Stephen J. Harris, Nigel P. Brandon, and Volder Schmidt. Stochastic simulation model for the 3d morphology of composite materials in Li-ion batteries. *Computational Materials Science*, 50:3365–3376, 2011.
[116] Indrajeet V. Thorat, Tapesh Joshi, Karim Zaghib, John N. Harb, and Dean R. Wheeler. Understanding rate-limiting mechanisms in lifepo4 cathodes for li-ion batteries. *Journal of the Electrochemical Society*, 158(11):A1185–A1193, 2011.
[117] Indrajeet V. Thorat, David E. Stephenson Nathan A. Zacharias, Karim Zaghib, John N. Harb, and Dean R. Wheeler. Quantifying tortuosity in porous Li-ion battery materials. *Journal of Power Sources*, 188:592–600, 2009.
[118] William Tiedemann and John Newman. Double-layer capacity determination of porous electrodes. *Journal of the Electrochemical Society*, 122(1):70–74, 1975.
[119] Salvatore Torquato. *Random Heterogeneous Materials Microstructure and Macroscopic Properties*, volume 16 of *Interdisciplinary Applied Mathematics*. Springer, 2002.
[120] Lars Ole Valoen and Jan N. Reimers. Transport properties of lipf6-based li-ion battery electrolytes. *Journal of the Electrochemical Society*, 152(5):A882–A891, 2005.
[121] Katja Weichert, Wilfried Sigle, Peter A. van Aken, Janez Jamnik, Changbao Zhu, Ruhul Amin, Tolga Acarturk, Ulrich Starke, and Joachim Maier. Phase boundary propagation in large lifepo4 single crystals on delithiation. *J. Am. Chem.Soc.*, 134:2988–2992, 2012.
[122] K. West, T. Jacobsen, and S. Atlung. Modeling of porous insertion electroes with liquid electrolyte. *Electrochemical Science and Technology*, 129(7):1480–1485.
[123] Yujie Zhu and Chunsheng Wang. Galvanostatic intermittent titration technique for phase-transformation electrodes. *Journal of Physical Chemistry C*, 114:2830–2841, 2010.

IX. TABLES

X. FIGURES

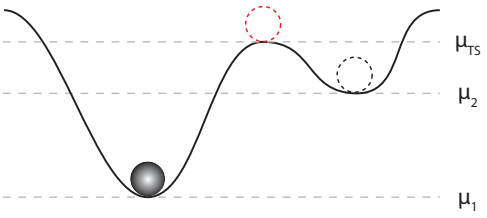

FIG. 1. **Typical reaction energy landscape**. This figure demonstrates a typical energy landscape for a reaction. The particle travels through a transition state as it passes from one state to the other.

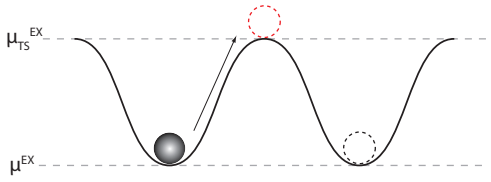

FIG. 2. **Typical diffusion energy landscape**. This figure demonstrates a typical energy landscape for a particle diffusing. When considering the diffusivity, it is the excess chemical potential that plays a large role, since in the dilute limit, diffusivity is roughly constant.

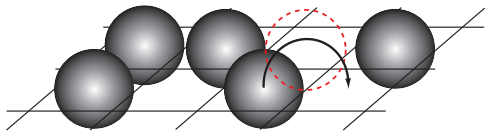

FIG. 3. **Lattice gas model for diffusion**. This figure demonstrates the lattice gas model. The particles are assumed to be hard spheres and each occupy a space on the grid. Particles can only jump to an open space, and the transition state (red dashed circle) requires two empty spaces.

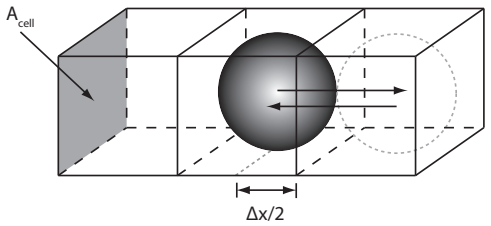

FIG. 4. **Diffusion through a solid**. This figure demonstrates how a particle diffuses through a lattice. The flux is given by the reaction rate across the area of the cell, A_{cell}.

Equation	Boundary Conditions
$\epsilon\frac{\partial c}{\partial t} + a_p j_{in} = \nabla\cdot(\epsilon D_{amb}\nabla c) - \nabla\cdot\left(\frac{t_+\mathbf{i}}{e}\right)$	$\mathbf{i}\big\|_{x=-\delta_s} = I/A_{sep}$
$\mathbf{i} = -e\left(D_+ - D_-\right)\epsilon\nabla c - \frac{e^2}{k_B T}\left(z_+ D_+ + z_- D_-\right)\epsilon c\nabla\phi$	
$j_{in} = -\frac{\nabla\cdot\mathbf{i}}{e a_p} = i_o\left[\exp\left(-\frac{\alpha e\eta}{k_B T}\right) - \exp\left(\frac{(1-\alpha)e\eta}{k_B T}\right)\right]$	
$i_o = \frac{e\left(k_c^o a_O\right)^{1-\alpha}\left(k_a^o a_R\right)^{\alpha}}{\gamma_\ddagger}$	
$\eta \equiv \Delta\phi - \Delta\phi_{eq}$	
$\Delta\phi_{eq} = V^o - \frac{k_B T}{ne}\ln\left(\frac{a_R}{a_O}\right)$	
$\frac{\partial c_s}{\partial t} = \nabla\cdot\left(\frac{D_s c_s}{k_B T}\nabla\mu\right)$	$-\frac{D_s c_s}{k_B T}\frac{\partial\mu}{\partial r}\Big\|_{r=R} = j_{in}$

TABLE I. **Dimensional set of equations**. This table lists the set of dimensional equations for Modified Porous Electrode Theory.

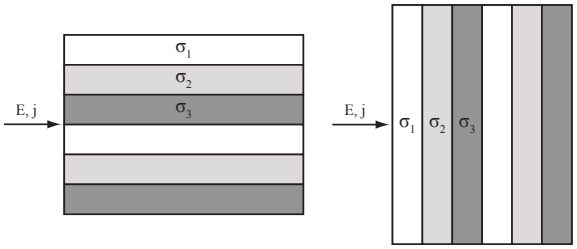

FIG. 5. **Upper and lower limit for anisotropic material**. The left figure demonstrates the upper conductivity limit for an anisotropic material. The arrangement of the materials acts like resistors in parallel. The right figure demonstrates the lower limit, with the materials arranged to act like resistors in series.

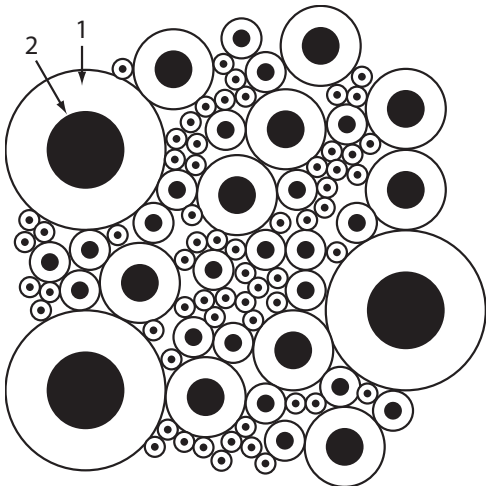

FIG. 6. **Hashin-Shtrikman bounds model**. Isotropic composite of coated spheres. The white represents material with conductivity σ_1 and the bloack represents material with conductivity σ_2. Maximum conductivity is achieved when $\sigma_1 > \sigma_2$ and minimum conductivity is obtained when $\sigma_2 > \sigma_1$. The upper and lower bounds are computed based on this. The volume fractions Φ_1 and Φ_2 are the same.

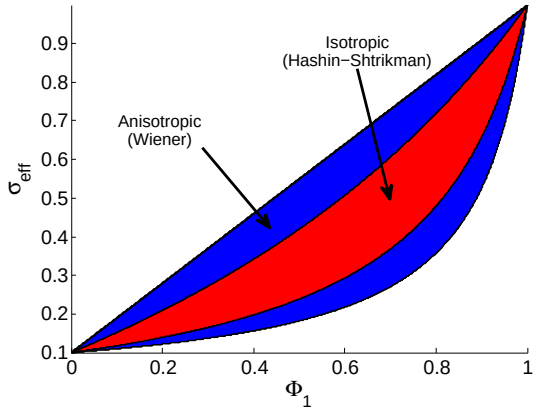

FIG. 7. **Conductivity bounds for two material composite**. The above figure shows the Wiener bounds (blue) for an anisotropic two component material and Hashin-Shtrikman bounds (red) for an isotropic two component material versus the volume fraction of material 1. The conductivities used to produce the figure are $\sigma_1 = 1$ and $\sigma_2 = 0.1$.

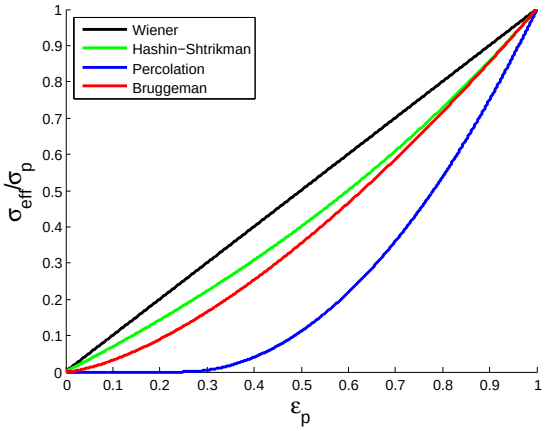

FIG. 8. **Various models for effective conductivity in 3D**. This figure demonstrates the effective conductivity (scaled by the pore conductivity) using Wiener bounds, Hashin-Shtrikman bounds, a percolation model, and the Bruggeman formula. The percolation model uses a critical porosity of $\epsilon_c = 0.25$.

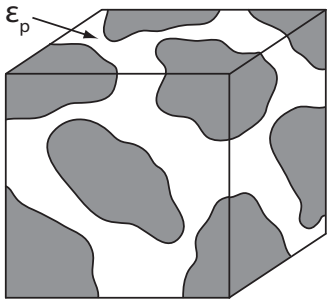

FIG. 9. **Example of a porous volume**. This is an example of a typical porous volume. A mixture of solid particles is permeated by an electrolyte. The porosity, ϵ_p, is the volume of electrolyte as a fraction of the volume of the cube.

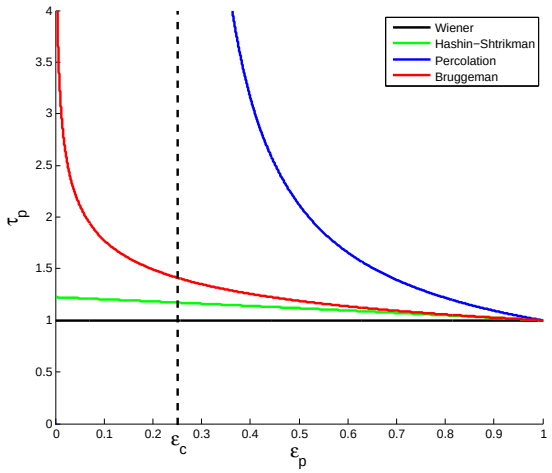

FIG. 10. **Tortuosity versus porosity for different effective conductivity models**. This plot gives the tortuosity for different porosity values. While the Wiener and Hashin-Shtrikman models produce finite tortuosities at 0 porosity, the percolation and Bruggeman models diverge.

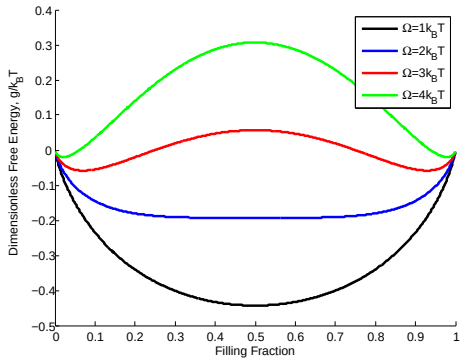

FIG. 11. **Regular solution model of free energy**. This figure shows the effect of the regular solution parameter on the free energy. For $\Omega < 2k_BT$, there is a single minimum. For $\Omega > 2k_BT$, there are two minima. This produces phase separation, as the system is unstable with respect to infinitesimal perturbations near the spinodal concentration, which is where the curvature of the free energy changes.

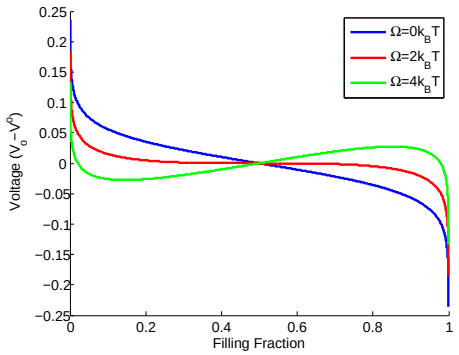

FIG. 12. **Open circuit potential for different regular solution parameter values**. The figure demonstrates various open circuit potentials for different regular solution parameter values. Notice how the voltage curve is non-monotonic when the system is phase separating.

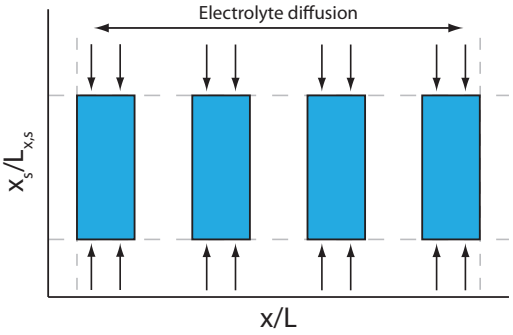

FIG. 13. **Plot axes for homogeneous particles**. This figure shows how the data for homogeneous particles is plotted. The y-axis of the contour plots represent the depth of the particles while the x-axis represents the depth into the electrode. The particles are modeled in 1D.

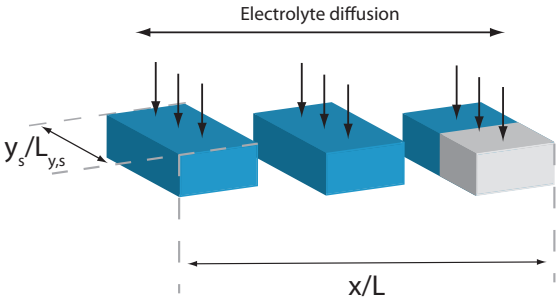

FIG. 14. **Plot axes for phase separating particles**. This figure shows how the data for phase-separating particles is plotted. The y-axis of the contour plots represent the length along the surface of the particle, since diffusion is assumed to be fast in the depth direction. The x-axis represents the depth in the electrode.

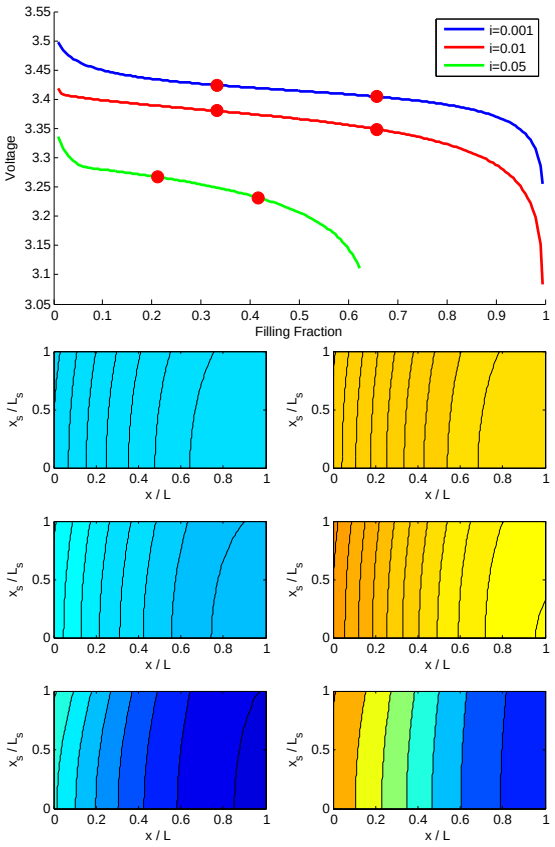

FIG. 15. **Effect of current on homogeneous particles**. This figure demonstrates the effect of different discharge rates on the voltage profile. The non-dimensional currents correspond to roughly C/3, 3C, and 15C. The solid diffusion is fast, with $\delta_d = 1$.

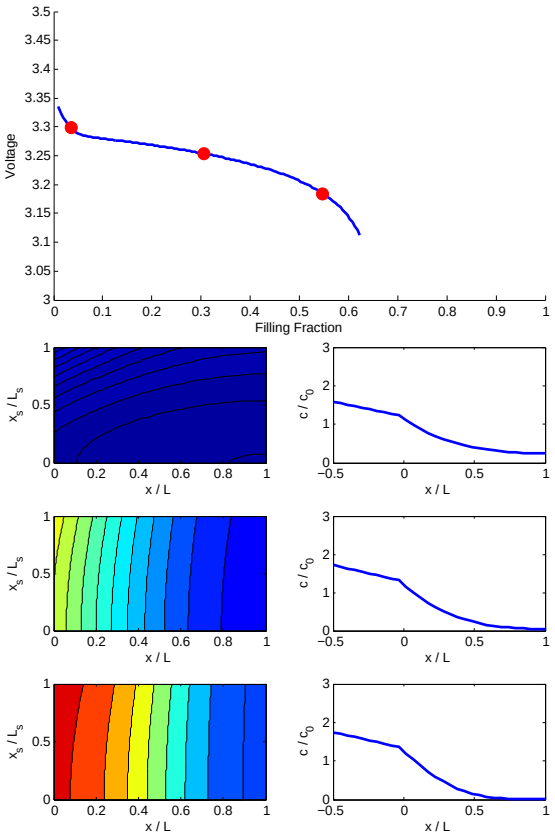

FIG. 16. **Depletion of the electrolyte at higher current**. This figure shows the depletion of the electrolyte accompanying Figure 15 for the 15C discharge. The left figure shows the solid concentration while the right figure demonstrates the electrolyte concentration profile in the separator and electrode.

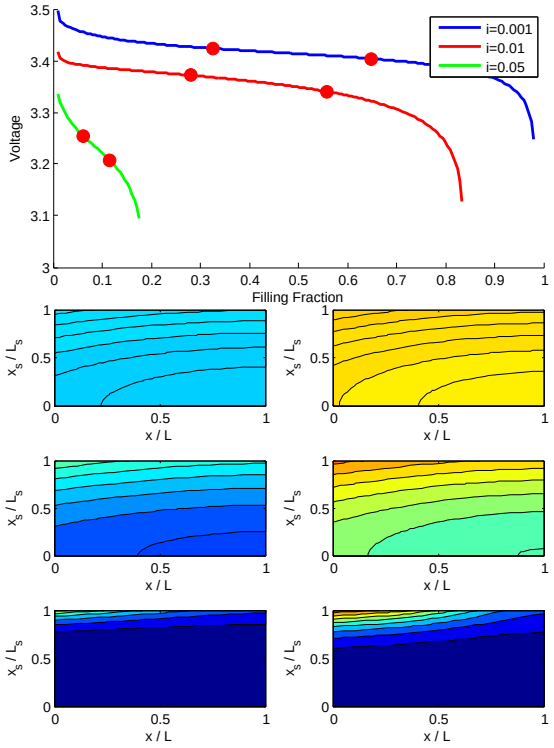

FIG. 17. **Effect of current on homogeneous particles with slower solid diffusion**. This figure demonstrates the effect of different discharge rates on the voltage profile. The non-dimensional currents correspond to roughly C/3, 3C, and 15C. The solid diffusion is slower than the electrolyte diffusion ($\delta_d = 50$).

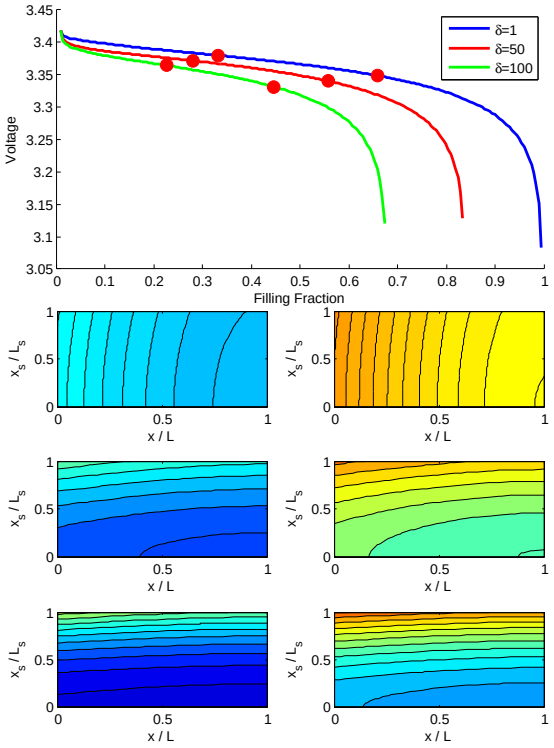

FIG. 18. **Effect of solid diffusivity on homogeneous particles**. This figure demonstrates the effect of decreasing solid diffusivity on the voltage profile. Each of these simulations was run at a dimensionless exchange current density of 0.01 and a dimensionless current of 0.01.

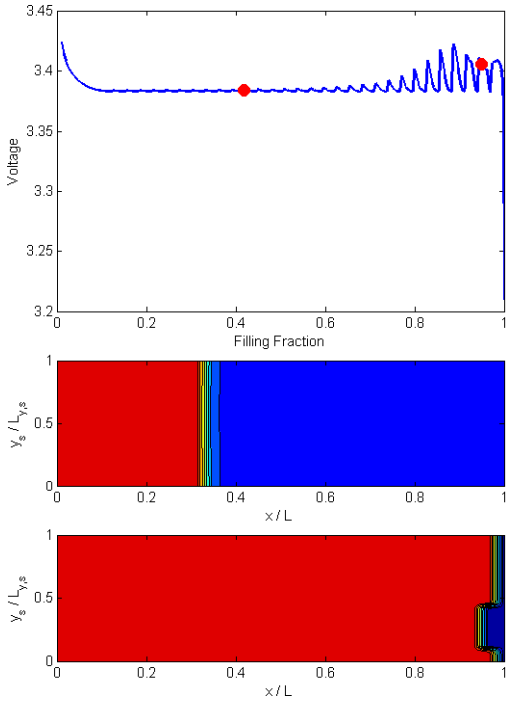

FIG. 19. **Phase separating particles slowly discharged**. This figure shows slowly discharge (approx. C/30) phase separating particles. Adequate electrolyte diffusion and discrete filling don't allow time for the particles to phase separate early on. At the end of the discharge, sufficient time allows the particles to phase separate.

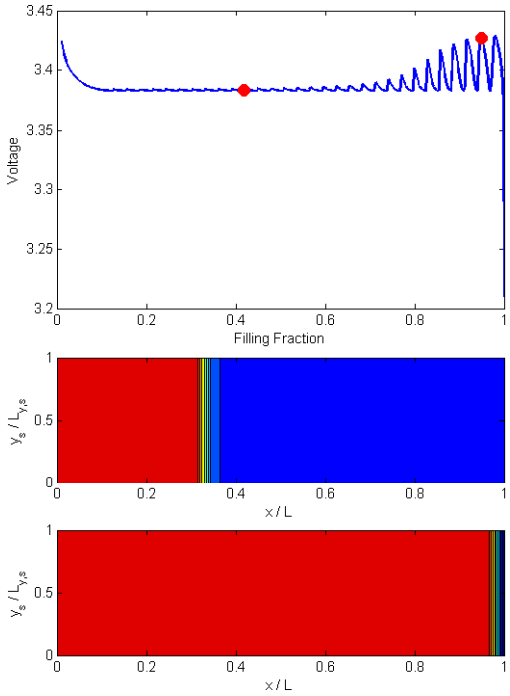

FIG. 20. **Phase separating particles including coherent stress effects slowly discharged**. This figure shows slowly discharge (approx. C/30) phase separating particles. The inclusion of the coherent stress effects suppresses phase separation inside the particles. This figure is the same as Figure 19, with an additional coherent stress term.

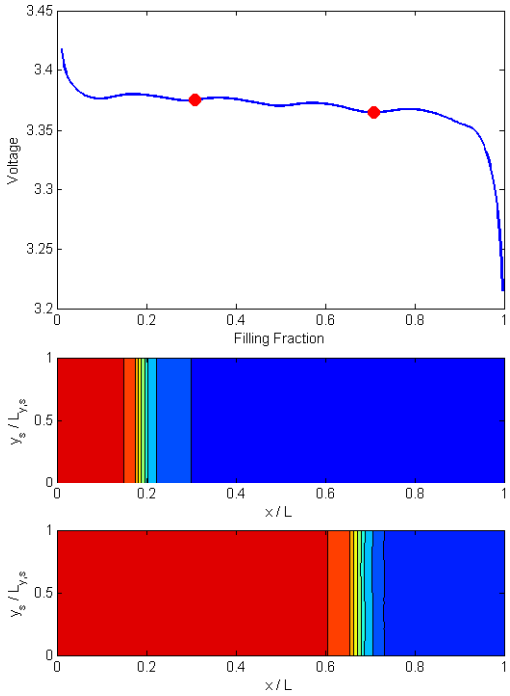

FIG. 21. **Effect of current on phase separating particles**. When the OCP is non-monotonic, the cell behavior varies with the discharge rate. At slow discharge, parts of the electrode fill discretely, creating voltage spikes on the order of the thermal voltage. When the cell is discharge quickly, this effect is suppressed, resulting in homogeneous filling of the particles.

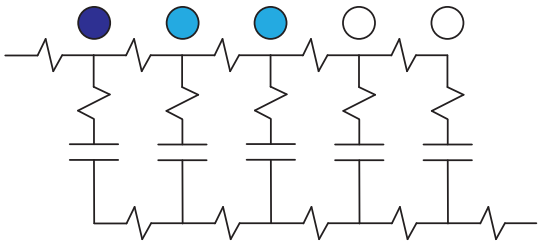

FIG. 22. **Equivalent circuit model for porous electrode**. This equivalent circuit represents a typical porous electrode. Resistors represent the contact, transport, and charge transfer resistances, and the capacitance of the particles is represented by a capacitor. All elements are not necessarily linear.